step scale as standard [3,4,6]. The index corresponding to bone mineral density (m-BMD) was obtained as the integrated value of the density area in X-ray film derived by the width of metacarpal bone. It was calculated that CV of m-BMD was 1.2–2.0% and m-BMD reflects the cortical density of the metacarpal bone [6].

### 3.3. Statistical analysis

The results were expressed as the mean ± S.E. Student's unpaired $t$-test and a one-way ANOVA analysis of variance test were used for statistical analysis. To test the relationship between two indices, Spearman's correlation coefficient test was performed. Differences were accepted as significant at $p < 0.05$.

## 4. Results

### 4.1. Urinary excretion of CPR, circulating levels of insulin, calcium, inorganic phosphorus, magnesium, i-PTH, 1,25(OH)$_2$D$_3$, and bone mineral density

Table 2 shows urinary excretion of CPR, circulating values of insulin, minerals, i-PTH and 1,25(OH)$_2$D$_3$ along with m-BMD in type 2 diabetic patients and in the controls. Urine levels of CPR were significantly reduced in type 2 diabetic patients compared to those in control subjects ($p < 0.01$). On the other hand, fasting levels of serum insulin tended to be higher in the diabetics, but no statistical

difference was observed between the diabetic and control groups. Serum levels of corrected calcium and magnesium were significantly lower in the diabetic group than in the controls ($p < 0.05$–$0.01$), but serum inorganic phosphorus was not significantly different. Serum i-PTH and 1,25(OH)$_2$D$_3$ were significantly decreased in diabetic patients than in their controls ($p < 0.01$). The values of m-BMD were significantly lower in the diabetic group compared to the control group ($p < 0.05$), indicating the decreased bone mass in the diabetic state.

### 4.2. Serum i-OC, TRAP, OCIF/OPG and urinary excretion of CTx, DPD, and NTx

Serum level of i-OC in type 2 diabetic patients was 0.53 ± 0.03 nmol/l, which was significantly lower than those in the controls (1.02 ± 0.05 nmol/l, $p < 0.01$). On the other hand, serum levels of TRAP in type 2 diabetic patients were 10.75 ± 0.14 U/l, and were significantly higher than those in the control group (9.50 ± 0.10 U/l, $p < 0.01$) (Fig. 1). Serum OCIF/OPG in diabetic patients (9.05 ± 0.45 pmol/l) tended to be higher than that in the control group (8.00 ± 0.31 pmol/l), although it is not statistically significant (0.05 < $p$ < 0.1). In addition, urinary concentrations of CTx, DPD, and NTx in type 2 diabetic patients were 161 ± 8 nmol/mMcre, 4.80 ± 0.13 nmol/mMcre and 41.9 ± 2.0 nMBCE/mMcre, respectively, and were also significantly higher than those in the control group (136 ± 6, 4.13 ± 0.13 nmol/mMcre, and 34.6 ± 1.5 nMBCE/mMcre, respectively; $p < 0.05$–$0.01$) (Fig. 2).

Table 2
Urine levels of CPR, circulating values of insulin and bone metabolic markers, and bone mineral density in male type 2 diabetic patients and their age-matched controls

|  | Type 2 diabetics | Controls |
| --- | --- | --- |
| Urine CPR (nmol/day) | 20.7 ± 1.3[a] | 30.0 ± 3.3 |
| Insulin (pmol/l) | 46.8 ± 2.5 | 37.8 ± 3.6 |
| Corrected calcium (mmol/kg albumin) | 5.08 ± 0.05[a] | 5.31 ± 0.04 |
| Inorganic phosphorus (mmol/l) | 1.05 ± 0.01 | 1.04 ± 0.02 |
| Magnesium (mmol/l) | 0.81 ± 0.01[b] | 0.83 ± 0.01 |
| Intact PTH (pmol/l) | 2.38 ± 0.10[a] | 3.26 ± 0.10 |
| 1,25 (OH)$_2$D$_3$ (pmol/l) | 101.3 ± 5.5[a] | 131.9 ± 7.3 |
| m-BMD (mmAl) | 2.80 ± 0.15[b] | 3.11 ± 0.03 |

Values were presented as mean ± S.E.
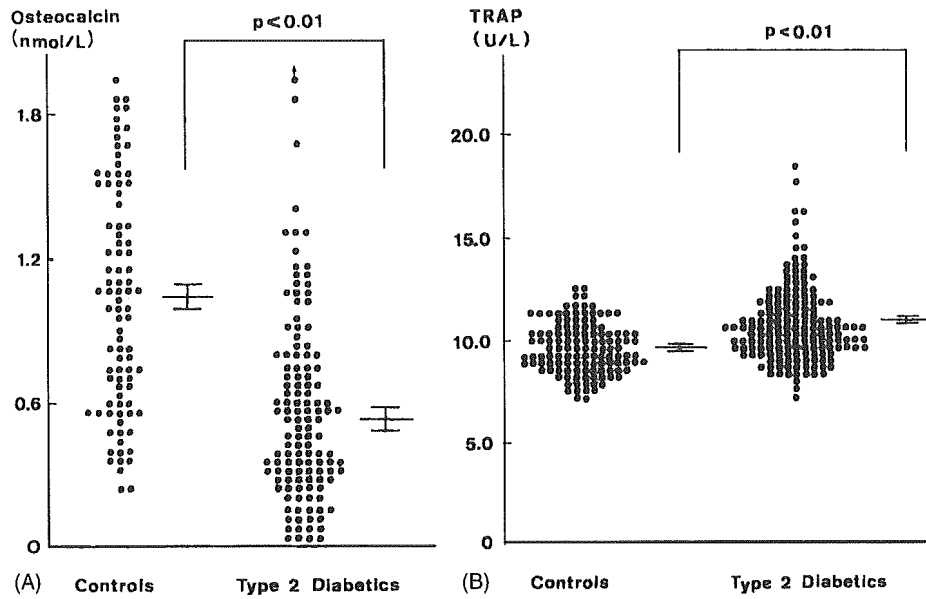[a] $p < 0.01$.
[b] $p < 0.05$ vs. control.

Fig. 1. Serum levels of i-OC (A), and TRAP (B) in type 2 diabetic patients and control subjects. Level of i-OC in the type 2 diabetics was significantly lower than that of the controls ($p < 0.01$). On the other hand, serum level of TRAP in the diabetics was higher than the value in their controls ($p < 0.01$).
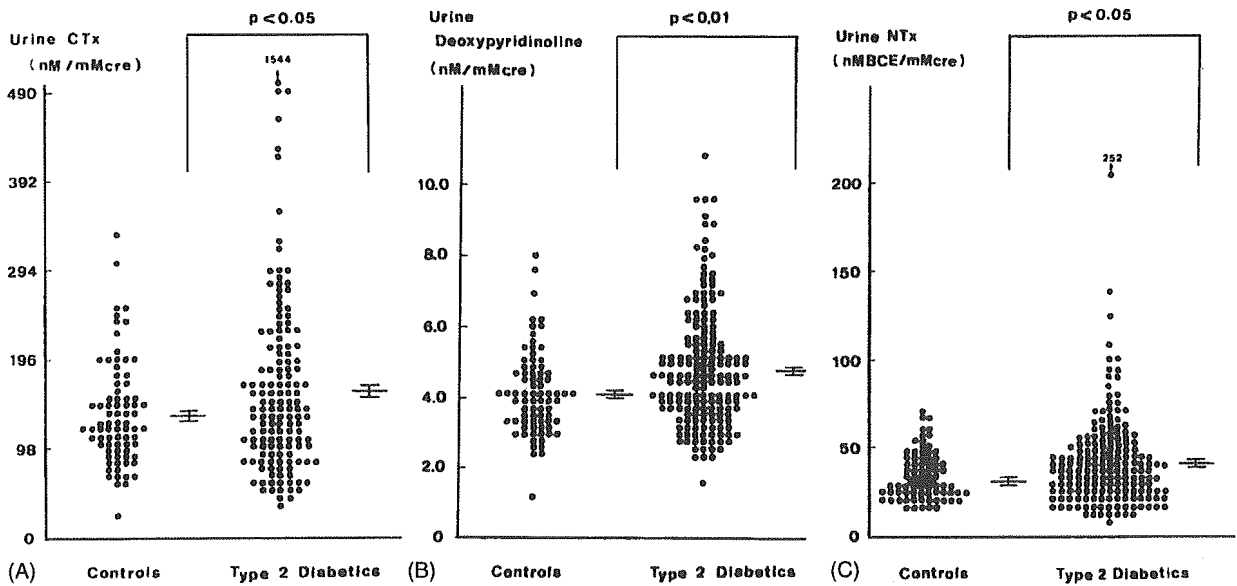


Fig. 2. Urine levels of CTx to creatinine (A), deoxypyridinoline (DPD) to creatinine (B), and NTx to creatinine (C) in type 2 diabetic patients and control subjects. Urine concentration of CTx and NTx in the type 2 diabetics was significantly higher than that in their controls ($p < 0.05$). Urine DPD in the diabetic group was also significantly higher than the value in their control group ($p < 0.01$).

### 4.3. Correlation coefficients among serum i-PTH and i-OC, serum and urine osteoclastic markers, and m-BMD in diabetic patients

A significantly positive correlation was found in diabetic patients between serum i-PTH and i-OC ($r = 0.289$, $p < 0.01$). There was no clear correlation between serum i-OC and TRAP. On the other hand, serum TRAP exhibited significantly positive correlation with urine osteoclastic markers (CTx and DPD) ($r = 0.298$ and $0.250$, respectively; $p < 0.01$). A significantly negative correlation was observed between m-BMD and serum levels of TRAP ($r = -0.254$, $p < 0.01$). The urinary excretion of CTx, DPD, and NTx similarly exhibited a tendency to be negatively correlated with m-BMD ($r = -0.211$, $-0.179$, and $-0.162$, respectively).

### 4.4. Correlationship between serum OCIF/OPG and serum i-OC, TRAP or m-BMD in diabetic patients

There was a significantly positive correlation in diabetic patients between circulating levels of OCIF/OPG and TRAP ($p < 0.01$; Fig. 3). The urinary excretion of CTx and DPD similarly tended to be negatively correlated with serum levels of OCIF/OPG ($r = -0.164$ and $-0.103$, respectively, $0.05 < p < 0.1$). On the other hand, a significantly negative correlation was found between m-BMD and serum OCIF/OPG ($p < 0.01$). There was no clear correlation between circulating levels of OCIF/OPG and i-OC (Fig. 3).

## 5. Discussion

The existence of diabetic osteopenia and altered mineral metabolism has been recognized as one of the chronic complications of diabetes mellitus [1–8]. In type 1 diabetic patients, fairly uniform results were obtained, where bone mass is reduced by 6–14% in the forearm [4]. Although many reports have been published to elucidate pathophysiological characteristics of abnormal bone metabolism in type 2 diabetic patients, however no detailed consensus on the pathogenesis of osteopenia in type 2 diabetes has been yet obtained. Differences in the race, age, sex and degree of obesity of the subjects in these studies can be considered as the causal factors of this inconsistency
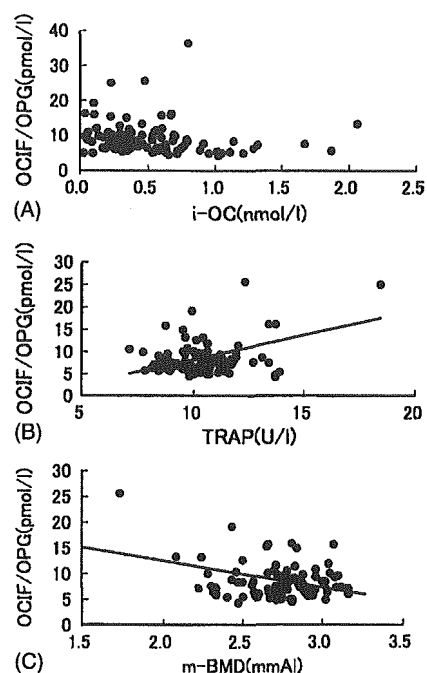


Fig. 3. Correlationship between serum OCIF/OPG (y-axis) and serum i-OC (A), TRAP (B) or m-BMD (C) (x-axis) in diabetic patients. There was a significantly positive correlation between circulating OCIF/OPG and TRAP ($r = 0.344$, $y = 2.72 + 1.10x$, $p < 0.01$), whereas no significant relationship was observed between serum OCIF/OPG and i-OC. On the other hand, a significantly negative correlation was found between serum OCIF/OPG and m-BMD ($r = -0.302$, $y = 22.97 - 5.21x$, $p < 0.01$).

[4,24,25]. Therefore, in the present study, only non-obese male patients with type 2 diabetes and their age-matched control subjects were examined in order to prevent the influence of sex, age and obesity from the evaluations of altered bone metabolism. The decreased activity of osteoblasts under diabetic conditions has been commonly observed in both diabetic animals and humans [7,26–28]. Since a positive correlation was found between i-PTH and i-OC, it is speculated that the relative hypofunction of parathyroid gland causes the decreased activity of diabetic osteoblasts. However, it has been still controversial if the osteoclastic function in diabetes is elevated or not [5,7,29,30]. We have previously reported that serum level of osteoblastic osteocalcin was decreased, while circulating TRAP, a bone resorption marker, was conversely elevated in genetically diabetic Wistar fatty rats [20], suggesting

the increased activity of osteoclasts in diabetic state. Moreover, in male type 2 diabetic patients, we found in the present study that serum concentrations of TRAP was significantly higher than those in age-matched controls, and that a significantly negative correlation was observed between serum TRAP and bone mineral content. A significant decrease in serum osteocalcin was conversely observed in the identical cases of type 2 diabetic patients, and there was no clear correlation between i-OC and TRAP. Thus, the accelerated osteoclastic activities and the putative uncoupling between the functions of osteoblasts and of osteoclasts would be supposedly related to the pathogenesis of diabetic osteopenia.

In order to ascertain the fact that osteoclastic activity in diabetic patients is increased, urinary excretion of CTx, DPD, and NTx was simultaneously examined. CTx and NTx have been known to be the cross-linked C- and N-terminal telopeptide of bone type I collagen and to be released into blood stream after the degradation of collagen through osteoclast-derived proteases [31]. Since CTx, DPD, and NTx are excreted from the kidney into urine, urinary con-centrations of these substances has been used as the means for estimation of osteoclastic bone resorption [10,32]. The urinary excretion of CTx and DPD was found to be elevated in the diabetic group and to be positively correlated with serum levels of TRAP. These results comfirm that the osteoclastic activity is significantly increased in type 2 diabetic patients.

It has been recognized that OCIF/OPG modifies osteoclastic differentiation by binding to ODF as decoy receptor, and then suppresses the generation of mature osteoclasts from their precurcer cells [33]. In addition, it has been reported that recombinant OCIF/OPG inhibits osteoclastogenesis in a dose-dependent manner in vitro, and increases bone mineral density and bone volume in vivo, associated with a decrease of active osteoclast number in normal rats [34]. In our studies, unexpectedly, the circulating levels of OCIF/OPG tended to be rather increased in type 2 diabetic patients. On the other hand, serum OCIF/OPG exhibited significantly positive correlation with serum TRAP, so that, it is possible that OCIF/OPG plays a protective role against the increased bone resorption under diabetic condition. In addition, a negative correlation between OCIF/OPG and m-BMD might be related to the putative role of this osteoblast-derived

cytokine to prevent further loss of the bone mass in diabetic patients.

It has been reported that serum OCIF/OPG is very sensitive to renal function. For example, the age-related increase in serum OCIF/OPG is likely to be related to modest deterioration in glomerular filtration rate with age [35]. We excluded diabetic patients with evident renal dysfunction in this study. Furthermore, there was no significant correlation between serum OCIF/OPG and corrected urine albumin (data not shown). Although it is true that OCIF/OPG is osteoblast-derived, OCIF/OPG has other roles, and the majority of plasma OCIF/OPG is likely to be derived from not only bone but also other various tissues [36]. In particular, OCIF/OPG has been reported to be involved in vascular physiology and its pathology [14]. In our preliminary study, however, no significant difference in serum levels of OCIF/OPG was found among the patients with various stages of diabetic retinopathy or neuropathy (data not shown). It is still unclear whether the etiological background is common in diabetic osteopenia and various kinds of vasculopathy in type 2 diabetic patients, because the examination on those with microvascular and macro-vasular complications were not performed in the present study. Further investigation will be needed in order to resolve the relationship between OCIF/OPG and diabetic vasculopathy.

The clinical management of diabetic osteopenia would become important for the preservation of quality of life in older diabetic patients, because it has been recently recognized that metabolic derangement under diabetic condition is related to the risk of bone fracture [37]. Further efforts should be necessary to clarify the detailed underlying mechanism and to establish the preventive methods for osteopenia in diabetic patients.

# References

[1] J. Me Levin, C. Vincenza, VC. Boisseau, L.V. Avioli, Effects of diabetes mellitus on bone mass in juvenile and adult-onset diabetes, N. Eng. J. Med. 294 (1976) 241–245.

[2] P. McNair, S. Madsbad, C. Christiansen, O.K. Faber, I. Trans-bøl, C. Binder, Osteopenia in insulin treated diabetes mellitus. Its relation to age at onset, sex and duration of disease, Diabetologia 15 (1978) 87–90.

[3] H. Ishida, Y. Seino, S. Matsukura, et al. Diabetic osteopenia and circulating levels of vitamin D metabolites in type 2 (noninsulin-dependent) diabetes, Metabolism 34 (1985) 797–801.

[4] Y. Seino, H. Ishida, Diabetic osteopenia: pathophysiology and clinical aspects, Diabetes Metab. Rev. 11 (1995) 21–35.

[5] R. Okazaki, Y. Totsuka, K. Hamano, et al. Metabolic improvement of poorly controlled noninsulin-dependent diabetes mellitus decreases bone turnover, J. Clin. Endocrinol. Metab. 82 (1997) 2915–2970.

[6] K. Suzuki, C. Sugimoto, M. Takizawa, et al. Correlation between bone mineral density and circulating bone metabolic markers in diabetic patients, Diabetes Res. Clin. Pract. 48 (2000) 185–191.

[7] K. Suzuki, Y. Taguchi, H. Ishida, Y. Seino, The evidence for uncoupling between bone formation and resorption in NIDDM patients, Diabetologia 40 (Suppl. 1) (1997) A581.

[8] R. Okazaki, M. Miura, M. Toriumi, et al. Short-term treatment with troglitazone decreases bone turnover in patients with type 2 diabetes mellitus, Endocr. J. 46 (1999) 795–801.

[9] M. Donde, C. Fledelius, P. Qvist, C. Christiansen, Coated-tube radioimmunoassay for C-telopeptides of type I collagen to assess bone resorption, Clin. Chem. 42 (1996) 1639–1644.

[10] D. Unbelhart, A. Schlemmer, J.S. Johansen, E. Gineyts, C. Christiansen, P. Delmas, Effect of menopause and hormone replacement therapy on the urinary excretion of pyridinium cross-links, J. Clin. Endocrinol. Metab. 72 (1991) 367–373.

[11] M.A. Da Hanson, A.M. Weis, S.L. Bollen, F.R. Maslan, D.R. Singer, Eyre Specific immunoassay for monitoring human bone resorption: quantitation of type I collagen cross-linked N-telopeptide in urine, J. Bone Miner. Res. 7 (1992) 1251–1258.

[12] D.M. Anderson, E. Marakovsky, W.L. Billingsley, et al. A homologue of the TNF receptor and its ligand enhance T-cell growth and dendric-cell function, Nature 390 (1997) 175–179.

[13] DL. Lacey, E. Timms, H.L. Tan, et al. Osteoprotegerin ligand is a cytokine that regulates osteoclast differentiation and activation, Cell 93 (1998) 165–176.

[14] E. Tsuda, M. Goto, S. Mochizuki, et al. Isolation of a novel cytokine from human fibroblasts that specifically inhibits osteoclastogenesis, Biochem. Biophys. Res. Commun. 234 (1997) 137–142.

[15] W.S. Browner, L.Y. Lui, S.R. Cummings, Associations of serum osteoprotegerin levels with diabetes, stroke, bone density, fractures, and mortality in elderly women, J. Clin. Endocrinol. Metab. 86 (2001) 631–637.

[16] K. Suzuki, H. Ishida, C. Sugimoto, et al. The urinary concentration of sialic acid is increased in non-insulin-dependent diabetic patients with microangipathy: a possible useful marker for diabetic microangiopathy, Diabetic Med. 12 (1995) 1092–1096.

[17] G. Mundy, R. Garrett, S. Harris, et al. Stimulation of bone formation in vitro and in rodents by statins, Science 286 (1999) 1946–1949.

[18] H. Ishida, K. Suzuki, Y. Someya, et al. Possible compensatory role of parathyroid hormone-related peptide on maintenance of calcium homeostasis in patients with non-insulin dependent diabetes mellitus, Acta Endocrinol. (Copenhagen) 129 (1993) 519–524.

[19] K. Nakashima, Y. Hattori, K. Yamazaki, et al. Immediate elimination of labile HbA1c with allosteric effectors of hemoglobin, Diabetes 39 (1990) 17–21.

[20] K. Takai, K. Nanaka, K. Ichihara, et al. Food constituents as a cause of variation of C-peptide excretion in the urine, Endocrinol. Jpn. 31 (1984) 291–299.

[21] K. Hosoda, H. Eguchi, T. Nakamoto, et al. Sandwich immunoassay for intact osteocalcin, Clin. Chem. 38 (1992) 2233–2238.

[22] K. Suzuki, H. Ishida, T. Takeshita, et al. Circulating levels of tartrate-resistant acid phosphatase in rat models of non-insulin-dependent diabetes mellitus, J. Diabetes Comp. 12 (1998) 176–180.

[23] W.D. Fraser, B.H. Durham, J.L. Berry, E.B. Mawer, Measurement of plasma 1, 25 dihydroxyvitamin D using a novel immunoextraction technique and immunoassay with iodine labeled vitamin D tracer, Ann. Clin. Biochem. 34 (1997) 632–637.

[24] PLA. Van Daele, R.P. Stolk, H. Burger, et al. Bone density in non-insulin-dependent diabetes mellitus, Ann. Intern. Med. 122 (1995) 409–414.

[25] J.C. Krakauer, M.J. Mckenna, N.F. Buderer, D.S. Rao, F.W. Whitehouse, A.M. Parfitt, Bone loss and bone turnover in diabetes, Diabetes 44 (1995) 775–782.

[26] S. Hough, L.V. Avioli, M.A. Bergfell, M.D. Fallon, E. Slatopolsky, S.L. Teitelbaum, Correction of abnormal bone and mineral metabolism in chronic streptozotocin-induced diabetes mellitus in the rat by insulin therapy, Endocrinology 108 (1981) 2228–2234.

[27] H. Ishida, Y. Seino, T. Taminato, et al. Circulating levels and bone contents of bone γ-carboxyglutamic acid-containing protein are decreased in streptozotocin-induced diabetic osteopenia, Diabetes 37 (1988) 702–706.

[28] N. Takeshita, H. Ishida, T. Yamamoto, et al. Circulating levels of and bone contents of bone γ-carboxyglutamic acid-containing protein in rat models of noninsulin-dependent diabetes mellitus, Acta Endocrinol. (Copenhagen) 128 (1993) 69–73.

[29] J. Verhaegue, A.M. Suiker, T.A. Einhorn, et al. Brittle bones in spontaneously diabetic female rats cannot be predicted by bone mineral measurements: Studies in diabetic and ovariectomized rats, J. Bone Miner. Res. 9 (1994) 1657–1667.

[30] B. Piekorn, P. Kann, T. Forst, J. Andreas, A. Ptützner, J. Beyer, Bone mineral density and bone metabolism in diabetes mellitus, Horm. Metab. Res. 29 (1997) 204–219.

[31] C. Fledelius, A.H. Johnsen, P. Cloos, M. Bonde, P. Qvist, Characterization of urinary degradation products derived from type I collagen, J. Biol. Chem. 272 (1997) 9755–9763.

[32] A. Colwell, R.G.G. Russell, R. Eastell, Factors affecting the assay of urinary 3-hydroxypyridinium crosslinks of collagen as markers of bone resorption, Eur. J. Clin. Invest. 23 (1993) 341–349.

[33] H. Yasuda, N. Shima, N. Nakagawa, et al. Osteoclast differentiation factor is a ligand for osteoprotegerin/osteoclastogenesis-inhibitory factor and is identical to TRANCE/RANKL, Proc. Natl. Acad. Sci. U.S.A. 95 (1998) 3597–3602.

[34] H. Yasuda, N. Shima, N. Nakagawa, et al. Identity of osteo-clastogenesis inhibitory factor (OCIF) and osteoprotegerin (OPG): a mechanism by which OPG/OCIF inhibits osteoclas-togenesis in vitro, Endocrinology 139 (1998) 1329–1337.

[35] JJ. Kazama, T. Shigematsu, K. Yano, et al. Increased circulting levels of osteoclastgenesis inhibitory factor (osteoprotegerin) in patients with chronic renal failure, Am. J. Kidney Dis. 39 (2002) 525–532.

[36] W.S. Simonet, D.L. Lacey, C.R. Dunsta, et al. Osteoprotegrin: a nobel secreted protein involved in the regulation of bone density, Cell 89 (1997) 309–319.

[37] A.V. Schwartz, D.E. Sellmeyer, K.E. Ensrud, et al. Older women with diabetes have an increased risk of fracture; a prospective study, J. Clin. Endocrinol. Metab. 86 (2001) 32–38.

Shinya Yamaguchi, Hiroshi Katahira, Sachihiko Ozawa, Yoko Nakamichi, Toshiaki Tanaka, Tatsuhiro Shimoyama, Kazuto Takahashi, Katsuhiko Yoshimoto, Mica Ohara Imaizumi, Shinya Nagamatsu and Hitoshi Ishida

You might find this additional information useful...

This article cites 31 articles, 23 of which you can access free at:
http://ajpendo.physiology.org/cgi/content/full/289/4/E643#BIBL

Updated information and services including high-resolution figures, can be found at:
http://ajpendo.physiology.org/cgi/content/full/289/4/E643

Additional material and information about *AJP - Endocrinology and Metabolism* can be found at:
http://www.the-aps.org/publications/ajpendo

This information is current as of April 5, 2006 .

# Activators of AMP-activated protein kinase enhance GLUT4 translocation and its glucose transport activity in 3T3-L1 adipocytes

Shinya Yamaguchi,[1] Hiroshi Katahira,[1] Sachihiko Ozawa,[1] Yoko Nakamichi,[2]
Toshiaki Tanaka,[1] Tatsuhiro Shimoyama,[1] Kazuto Takahashi,[1] Katsuhiko Yoshimoto,[1]
Mica Ohara Imaizumi,[2] Shinya Nagamatsu,[2] and Hitoshi Ishida[1]

[1]*Third Department of Internal Medicine and* [2]*Department of Biochemistry, Kyorin University, Mitaka, Tokyo, Japan*

Yamaguchi, Shinya, Hiroshi Katahira, Sachihiko Ozawa, Yoko Nakamichi, Toshiaki Tanaka, Tatsuhiro Shimoyama, Kazuto Takahashi, Katsuhiko Yoshimoto, Mica Ohara Imaizumi, Shinya Nagamatsu, and Hitoshi Ishida. Activators of AMP-activated protein kinase enhance GLUT4 translocation and its glucose transport activity in 3T3-L1 adipocytes. *Am J Physiol Endocrinol Metab* 289: E643–E649, 2005. First published May 31, 2005; doi:10.1152/ajpendo.00456.2004.—To determine whether the increase in glucose uptake following AMP-activated protein kinase (AMPK) activation in adipocytes is mediated by accelerated GLUT4 translocation into plasma membrane, we constructed a chimera between GLUT4 and enhanced green fluorescent protein (GLUT4-eGFP) and transferred its cDNA into the nucleus of 3T3-L1 adipocytes. Then, the dynamics of GLUT4-eGFP translocation were visualized in living cells by means of laser scanning confocal microscopy. It was revealed that the stimulation with 5-aminoimidazole-4-carboxamide-1-β-D-ribofuranoside (AICAR) and 2,4-dinitrophenol (DNP), known activators of AMPK, promptly accelerates its translocation within 4 min, as was found in the case of insulin stimulation. The insulin-induced GLUT4 translocation was markedly inhibited after addition of wortmannin ($P <$ 0.01). However, the GLUT4 translocation through AMPK activators AICAR and DNP was not affected by wortmannin. Insulin- and AMPK-activated translocation of GLUT4 was not inhibited by SB-203580, an inhibitor of p38 mitogen-activated protein kinase (MAPK). Glucose uptake was significantly increased after addition of AMPK activators AICAR and DNP ($P <$ 0.05). AMPK- and insulin-stimulated glucose uptake were similarly suppressed by wortmannin ($P <$ 0.05–0.01). In addition, SB-203580 also significantly prevented the enhancement of glucose uptake induced by AMPK and insulin ($P <$ 0.05). These results suggest that AMPK-activated GLUT4 translocation in 3T3-L1 adipocytes is mediated through the insulin-signaling pathway distal to the site of activated phosphatidylinositol 3-kinase or through a signaling system distinct from that activated by insulin. On the other hand, the increase of glucose uptake dependent on AMPK activators AICAR and DNP would be additionally due to enhancement of the intrinsic activity in translocated GLUT4 protein, possibly through a p38 MAPK-dependent mechanism.

glucose transporter 4; mitogen-activated protein kinase; phosphatidylinositol 3-kinase; enhanced green fluorescent protein

IT HAS BEEN ESTABLISHED that insulin-stimulated glucose uptake into adipocytes and skeletal myocytes involves the translocation of GLUT4 from an intracellular pool to the plasma membrane. The intracellular mechanism for the recruitment of GLUT4-containing vesicle into plasma membrane has been investigated, and it has been revealed that phosphatidylinositol 3-kinase (PI3K) plays a crucial role in insulin-stimulated GLUT4 translocation (7, 14, 24). However, little has been

elucidated concerning other mechanisms to enhance the GLUT4 translocation than the insulin signaling system.

AMP-activated protein kinases (AMPKs) have been known to act as a metabolic sensor in mammalian cells (9, 30). The kinase activity is enhanced by a relative increase in cellular AMP level (increase in AMP-to-ATP ratio) through a metabolic uncoupler, dinitrophenol (DNP), to decrease ATP concentration and by 5-aminoimidazole-4-carboxamide-1-β-D-ribofuranoside (AICAR), an adenosine analog. After entering into cells, AICAR is phosphorylated, and the reaction product 5-aminoimidazole-4-carboxamide ribonucleotide mimics the action of AMP to activate AMPK (6, 19). In the case of skeletal myocytes, activation of AMPK through physiological stimulation such as muscle contraction or by the pharmacological activator AICAR leads to a significant increase of glucose uptake mediated by the translocation of GLUT4 (10, 20).

It has been reported that GLUT4 translocation is accelerated by stimulation other than by insulin, such as hyperosmolar shock and bradykinin (2, 4, 15), but the precise mechanism has not yet been elucidated. In addition, although AMPK activation by AICAR in adipocytes has also been observed to increase glucose uptake under basal conditions (27), it seems to be still unclear whether or not its increase is mediated by GLUT4 translocation. In this study, we monitored in real time the GLUT4 trafficking in living, single 3T3-L1 adipocytes by use of a chimera between GLUT4 and the intrinsically fluorescent enhanced green fluorescent protein (eGFP). The time-dependent acceleration of GLUT4 translocation was measured using laser-scanning confocal microscopy after AMPK activation by AICAR and DNP. The effect of insulin was examined in parallel for a comparative purpose. The involvement of PI3K and p38 mitogen-activated protein kinase (MAPK) activation was also investigated in the mechanisms for accelerated GLUT4 translocation and increased glucose uptake through AMPK activation in 3T3-L1 adipocytes.

## MATERIALS AND METHODS

*Materials.* Wortmannin, AICAR, and bovine serum albumin (BSA) were from Sigma (St. Louis, MO), and DNP and 2-deoxy-D-glucose (2-DG) were from Wako (Osaka, Japan). SB-203850 was from Calbiochem (La Jolla, CA). 2-[$^{14}$C]DG (300 mCi/mmol) was obtained from DuPont-NEN (Boston, MA). Human GLUT4 cDNA was a generous gift from Dr. G. I. Bell (University of Chicago). The GLUT4-eGFP construct was prepared by subcloning the full-length GLUT4 cDNA in frame into the *Hind*III and *Eco*R1 sites of the peGFP vector (Clontech, Palo Alto, CA) to make a COOH-terminal eGFP fusion.

*Preparation of cells.* 3T3-L1 cells were obtained from the cell bank of Japanese Collection of Research Bioresouces (Tokyo, Japan). Cells were seeded and fed every 2–3 days in Dulbecco's modified Eagle's medium (DMEM) high glucose supplemented with 50 U/ml penicillin, 50 μg/ml streptomycin, 100 mM MEM sodium pyruvate, and 10% fetal calf serum and were grown under 5% $CO_2$ at 37°C. At confluence, differentiation was started by addition of medium containing 500 μM isobutylmethylxanthine (IBMX, Sigma), 250 μM dexameth-

asone (Sigma), and 1.7 μM insulin. After 48 h, this mixture was replaced with fresh medium. Between *days 7* and *10* after induction of differentiation, the glucose uptake was determined using 2-[$^{14}$C]DG, and the dynamics of GLUT4 translocation were monitored in living cells by transferring the cDNA of GLUT4-eGFP into their nucleus.

*Cell microinjection of GLUT4-eGFP cDNA.* 3T3-L1 adipocytes were injected with cDNA of GLUT4-eGFP using an Eppendorf microinjector system (Femtojet; Eppendorf, Hamburg, Germany) fit-
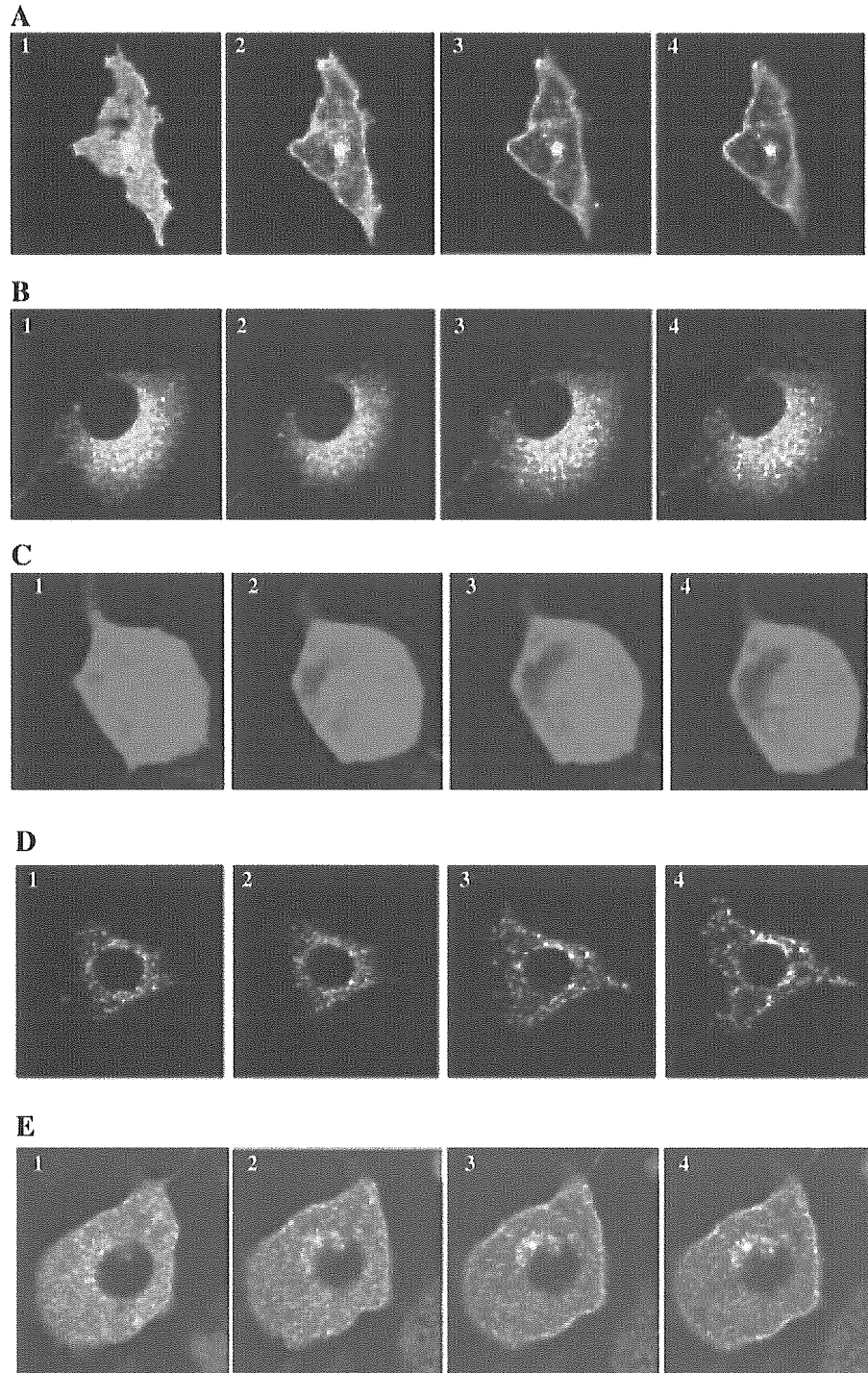


Fig. 1. Visualization of GLUT4 translocation using GLUT4-eGFP (enhanced green fluorescent protein) chimeric protein and dynamics of its intracellular distribution after addition of stimulants. Each image was obtained using laser-scanning confocal microscopy before (*1*), and 4 (*2*), 10 (*3*), and 20 min (*4*) after the following stimulations: *A*: $10^{-7}$ M insulin alone; *B*: $10^{-7}$ M insulin + 3 × $10^{-8}$ M wortmannin; *C*: $10^{-7}$ M insulin + $10^{-5}$ M SB-203580 (an inhibitor of p38 MAPK); *D*: $10^{-4}$ M 2,4-dinitrophenol (DNP) alone; *E*: $10^{-4}$ M DNP + 3 × $10^{-8}$ M wortmannin.

ted on to Zeiss Axiovert microscope. In each coverslip, the plasmid of GLUT4-eGFP cDNA adjusted to 50–200 μg/ml in 10 mM Tris·HCl buffer (pH 8.0) plus 1 mM EDTA was injected into the nucleus of ~50 cells. After injection, cells were washed twice with DMEM containing 10% fetal calf serum and incubated for 16–24 h under 5% $CO_2$ at 37°C. The efficiency of gene transfer into cells was in the range of 8–27%.

*Experimental protocol for stimulation with insulin, DNP, or AICAR.* After the preincubation of differentiated 3T3-L1 adipocytes in Krebs-Ringer bicarbonate (KRB) buffer containing (in mM) 110 NaCl, 4.4 KCl, 1.45 $KH_2PO_4$, 1.2 $MgCl_2$, 2.3 calcium gluconate, 4.8 $NaHCO_3$, 11 glucose, and 10 HEPES (pH 7.4) and 0.3% BSA (for GLUT4 translocation) or in serum-free Hanks' buffer (in mM: 136.9 NaCl, 5.6 KCl, 0.34 $Na_2HPO_4 \cdot 7H_2O$, 0.44 $KH_2PO_4$, 1.27 $CaCl_2$, and 4.2 $NaHCO_3$ and 0.02% BSA, pH 7.4) (for 2-DG uptake) at 37°C for 140 min, cells were then additionally incubated with $10^{-7}$ M insulin, $10^{-4}$ M DNP or $10^{-3}$ M AICAR for 20 min. In experiments where the PI3K inhibitor (3 × $10^{-8}$ M wortmannin) or the p38 MAPK inhibitor ($10^{-5}$ M SB-203085) was used, each agent was added to the buffer 20 min before the addition of insulin, DNP, or AICAR.

*Image capture of GLUT4 translocation and its analysis.* The transfected 3T3-L1 adipocytes with GLUT4-eGFP were imaged with a laser-scanning confocal microscope LSM 510 (Carl Zeiss, Jena, Germany) to monitor the dynamics of GLUT4 translocation. Transfected cells were on a heated stage adjusted to provide a temperature of 37°C in the bathing KRB buffer. Images were collected using 488-nm excitation wavelength every 1 min. The eGFP signals were analyzed with NIH Image software (version 1.61, National Institute of Mental Health, NIMH Public Inquiries, Bethesda, MD). To quantify the extent of GLUT4-eGFP translocation to the plasma membrane, the ratio of fluorescence intensity in the peripheral region to that in the remaining cellular fluorescence was calculated. The peripheral-to-cellular ratio in the basal state was expressed as 100(%), and the area under the curve during the 20-min stimulation was calculated for the quantitative comparison.

*2-DG uptake assay.* The differentiated 3T3-L1 adipocytes were serum starved using serum-free Hanks' buffer (pH 7.4) prior to glucose uptake experiments, as described above, and were preincubated for 140 min. For 2-DG uptake measurements, 0.2 μCi 2-[$^{14}$C]DG was then added to the medium containing 1 mM nonra-
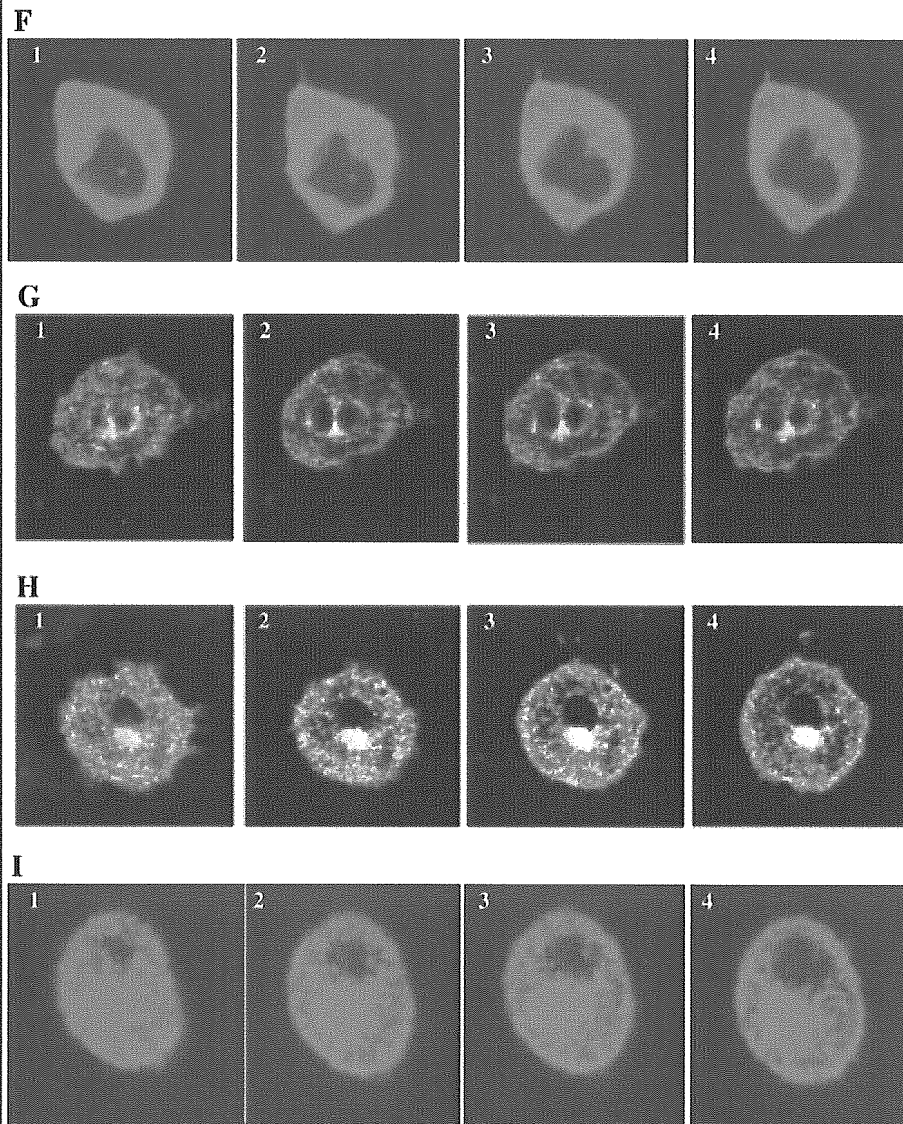
**F**



**G**



**H**



**I**



Fig. 1. *F:* $10^{-4}$ M DNP + $10^{-5}$ M SB-203580; *G:* $10^{-3}$ M 5-aminoimidazole-4-carboxamide-1-β-D-ribofuranoside (AICAR) alone; *H:* $10^{-3}$ M AICAR + 3 × $10^{-8}$ M wortmannin; *I:* $10^{-3}$ M AICAR + $10^{-5}$ M SB-203580.

dioactive 2-DG. After the incubation for 20 min at room temperature along with each stimulant (insulin, DNP, or AICAR), glucose uptake was stopped by aspiration of the buffer. Cells were rapidly washed several times with 1 ml of ice-cold phosphate-buffered saline and solubilized by the addition of 0.2 M NaOH. Nonspecific uptake was determined in parallel in the presence of 10 μM cytochalasin B. The radioactivity associated with the cells was measured using a scintillation counter (LSC-3100; Aloca, Tokyo, Japan), as has been described previously (21).

*Statistical analysis.* Statistical analysis was performed by analysis of variance using StatView computer software (Abacus, Berkeley, CA). Results are expressed as means ± SE, and $P < 0.05$ was considered significant.

## RESULTS

*Visualization of GLUT4 translocation and its dynamics of intracellular distribution.* The dynamics of GLUT4-eGFP translocation were visualized and monitored using laser-scanning confocal microscopy. Each image in Fig. 1 indicates the intracellular localization of GLUT4 before (1), and 4 (2), 10 (3), and 20 min (4) after the addition of $10^{-7}$ M insulin, $10^{-4}$ MDNP, or $10^{-3}$ M AICAR. As indicated in Fig. 1A, insulin stimulation elicited GLUT4 translocation into plasma membrane within 4 min. On the other hand, the time-dependent translocation was almost diminished by the pretreatment with $3 \times 10^{-8}$ M wortmannin (Fig. 1B). Administration of DNP or AICAR alone similarly promoted GLUT4 translocation within 4 min in a time-dependent manner (Fig. 1, D and G). The pretreatment with wortmannin, however, failed to inhibit the translocation by DNP or AICAR (Fig. 1, E and H). In addition, the translocation induced by insulin, DNP, or AICAR was not affected by the pretreatment with $10^{-5}$ M SB-203580. (Fig. 1, C, F, and I).

*Quantitative assessment of GLUT4 translocation by each stimulant.* A significant increase in the peripheral/cellular ratio of GLUT4-eGFP fluorescence intensity was observed 4 min after the addition of insulin (138.2 ± 13.3% of the basal state, $P < 0.05$), and it consistently continued thereafter ($P < 0.05$; Fig. 2A). When the cells were pretreated with wortmannin, however, no apparent acceleration of the GLUT4 translocation was found, and the statistically significant suppression was noted in the translocation during the insulin stimulation ($P < 0.05$; Fig. 2A). DNP and AICAR also significantly enhanced the GLUT4 translocation 4 min after the addition (140 ± 10.5 and 130.7 ± 8.5% of the basal state in DNP and AICAR stimulation, respectively, $P < 0.05$; Fig. 2, B and C). In contrast, the wortmannin pretreatment failed to suppress the GLUT4 translocation stimulated with DNP or AICAR (Fig. 2, B and C). The addition of SB-203580 did not suppress the translocation by insulin, DNP or AICAR (Fig. 2, A–C). When the area under the curve of peripheral/cellular ratio of fluorescence intensity was calculated (Fig. 3A), it was confirmed that wortmannin could almost completely inhibit the insulin-induced GLUT4 translocation (63,081 ± 8,516 and 181 ± 844 arbitary units in insulin alone and insulin plus wortmannin, respectively, $P < 0.01$), but not by DNP or AICAR (Fig. 3, B and C). No significant effect on the accelerated translocation by insulin, DNP, or AICAR was observed by the addition of SB-203580 (Fig. 3, A–C).

*Insulin-, DNP-, and AICAR-induced 2-DG uptake inhibition by wortmannin or SB-203580.* The stimulation by insulin, DNP, and AICAR enhanced 2-DG uptake 2.8 ± 0.14-, 2.4 ±



**A** insulin only / insulin + wortmannin / insulin +SB203580

**B** DNP only / DNP + wortmannin / DNP +SB203580

**C** AICAR only / AICAR + wortmannin / AICAR +SB203580
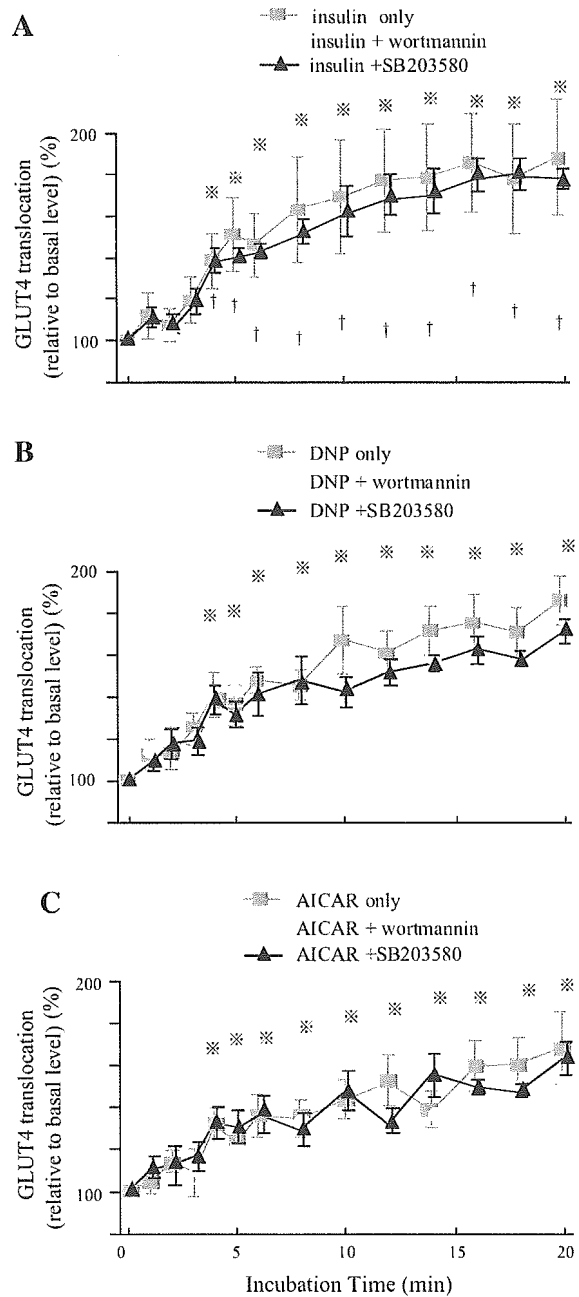
Incubation Time (min)

Fig. 2. Time course of quantified GLUT4 translocation in 3T3-L1 adipocytes after addition of $10^{-7}$ M insulin (A), $10^{-4}$ M DNP (B), and $10^{-3}$ M AICAR (C). These agents similarly elicited a significant increase of GLUT4 translocation 4 min after their addition. Wortmannin pretreatment markedly reduced the translocation induced by insulin but not that by DNP or AICAR. On the other hand, pretreatment with SB-203580 failed to affect all of them. *$P <$ 0.05 vs. nonstimulatory basal condition. †$P < 0.05$ vs. corresponding control. Data are means ± SE of 6 determinations on different 3T3-L1 cells.

0.21-, and 1.7 ± 0.14-fold, respectively ($P < 0.01$). The addition of wortmannin did not affect the basal 2-DG uptake but markedly suppressed the insulin-induced glucose uptake (5,215 ± 429 and 1,618 ± 277 cpm/$10^6$ cells in insulin alone and insulin plus wortmannin, respectively, $P < 0.01$). Inter-
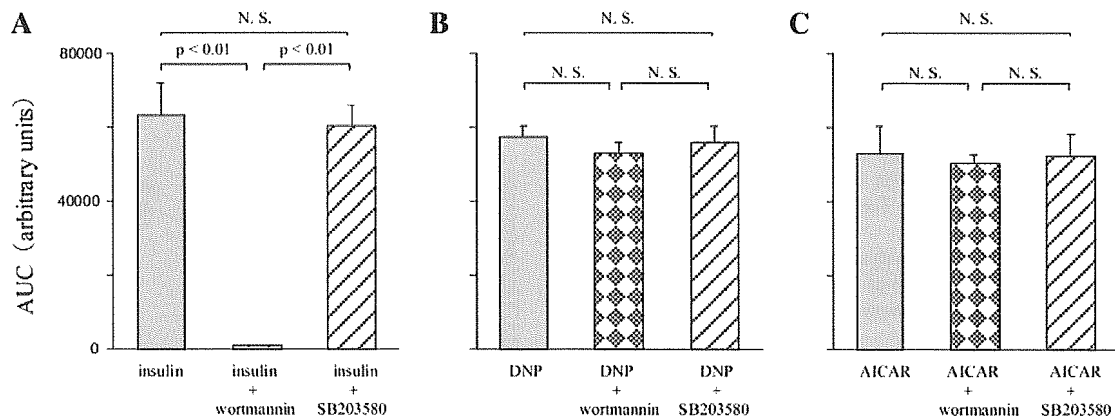
**Fig. 3.** Calculation of area under the curve (AUC) of %peripheral/cellular ratio of GLUT4-eGFP fluorescence intensity after addition of $10^{-7}$ M insulin (*A*), $10^{-4}$ M DNP (*B*), and $10^{-3}$ M AICAR (*C*). Accelerated GLUT4 translocation by insulin was significantly suppressed by $3 \times 10^{-8}$ M wortmannin ($P < 0.01$) but not by $10^{-5}$ M SB-203580. DNP- or AICAR-induced GLUT4 translocation was not affected by these agents. N.S., not significant. Data are means ± SE of 6 determinations on different 3T3-L1 cells.

estingly, wortmannin treatment could also significantly inhibit 2-DG uptake by DNP and AICAR (4,625 ± 555 and 2,903 ± 65 cpm/$10^6$ cells in DNP alone and DNP plus wortmannin, respectively, $P < 0.05$, and 3,140 ± 381 and 1,891 ± 150 cpm/$10^6$ cells in AICAR alone and AICAR plus wortmannin, respectively, $P < 0.05$; Fig. 4*A*), whereas wortmannin failed to suppress the GLUT4 translocation stimulated by these agents, as has been described above. In another series of experiments,

SB-203580 pretreatment was found to significantly inhibit the glucose uptake enhanced by insulin (5,752 ± 190 and 3,692 ± 67 cpm/$10^6$ cells in insulin alone and insulin plus SB-203580, respectively, $P < 0.05$) and also by DNP and AICAR (4,062 ± 212 and 3,072 ± 168 cpm/$10^6$ cells in DNP alone and DNP plus SB-203580, respectively, $P < 0.05$; 4,880 ± 316 and 2,444 ± 99 cpm/$10^6$ cells in AICAR alone and AICAR plus SB-203580, respectively, $P < 0.05$; Fig. 4*B*).
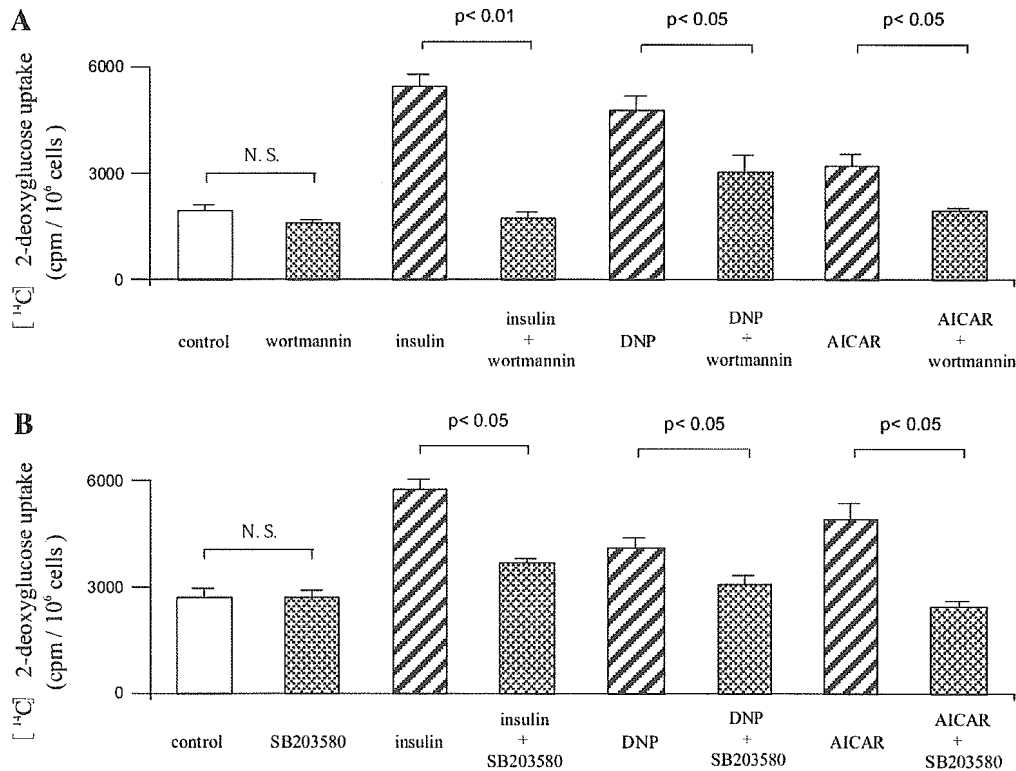


**Fig. 4.** Stimulation of glucose transport activity in 3T3-L1 adipocytes by insulin, DNP, and AICAR and its suppression by wortmannin (*A*) and SB-203580 (*B*). *A*: addition of wortmannin significantly reduced the glucose uptake stimulated by insulin, as well as that evoked by DNP and AICAR ($P < 0.05$–0.01). *B*: enhanced glucose uptakes by insulin, DNP, and AICAR were all significantly suppressed by addition of SB-203580 ($P < 0.05$). Data are means ± SE of 6 determinations.

## DISCUSSION

Through the monitoring system of visualized GLUT4-eGFP translocation (22, 25), we have demonstrated here that the stimulation with DNP and AICAR, known activators of AMPK, promptly promotes the GLUT4 translocation within 4 min, as has been previously reported in the case of insulin (13, 16, 23). In addition, the translocation induced by DNP and AICAR was not affected by wortmannin, suggesting that AMPK-stimulated GLUT4 translocation in 3T3-L1 adipocytes is mediated through the insulin-signaling pathway distal to the site of activated PI3K or through a signaling system distinct from that of insulin. This finding seems to be consistent with the case of enhanced GLUT4 translocation in skeletal muscles, in which AMPK activity has reportedly been elevated through their contraction (11, 17). Because the GLUT4 translocation induced by insulin stimulation and AMPK activation in 3T3-L1 adipocytes was not found to be affected by SB-203580, a known inhibitor of p38 MAPK, the recruitment of GLUT4 to the plasma membrane was unlikely to have been mediated by p38 MAPK signaling.

The addition of AMPK activators AICAR and DNP enhanced glucose uptake in 3T3-L1 adipocytes, as was found in the case of insulin stimulation. In contrast to the case of GLUT4 translocation, however, the glucose transport activity was significantly reduced by the addition of wortmannin. It has been supposed that the magnitude of glucose transport after insulin stimulation is regulated by promoting the GLUT4 translocation via PI3K activation (7, 14, 24) and also through increasing the intrinsic transport activity of GLUT4 by protein phosphorylation via p38 MAPK activation (3, 28, 29). Although wortmannin has been used as an inhibitor of PI3K, this agent has been additionally reported to inhibit insulin-dependent p38$\alpha$ and p38$\beta$ MAPK activities with an IC$_{50}$ of $6 \times 10^{-9}$ M and $2 \times 10^{-9}$ M, respectively (28). Because the concentration of wortmannin used in this experiment was $3 \times 10^{-8}$ M, it can be expected that it suppresses the p38 MAPK activities in 3T3-L1 adipocytes. In fact, the AMPK-activated glucose transport activity was found to be significantly suppressed by SB-203580 in the present study. Because the magnitude of the 2-DG transport response by insulin and AMPK activators was found to be relatively poor compared with that in previous studies (3, 29), the degree of cell differentiation of 3T3-L1 adipocytes might have been lower in our cell preparations. However, the significance in the reduction of glucose uptake by the addition of wortmannin and SB-203580 could still be valid, because apparent GLUT4 translocation into the plasma membrane of 3T3-L1 adipocytes was observed in the cell preparations similar to those in the glucose uptake assay. It could, accordingly, be speculated that the enhancement of glucose transport induced by AMPK activation in 3T3-L1 adipocytes is mediated by the increase of intrinsic activity through p38 MAPK activation of translocated GLUT4 protein, as has been suggested in the case of skeletal muscle (18). A detailed evaluation would be needed in the future regarding which isoforms of p38$\alpha$ and p38$\beta$ MAPK can be phosphorylated and activated during this process. However, because it has been demonstrated that SB-203580 inhibited the nucleotide transport system and therefore can indirectly reduce AICAR-stimulated AMPK activity (8), further examinations should be carefully conducted on the exact role of AMPK and p38

MAPK activation in the accelerated glucose uptake activity of GLUT4 protein in 3T3-L1 adipocytes. It has been recently reported that AICAR-stimulated glucose transport was dependent on activation of the extracellular signal-regulated kinase pathway, phospholipase D, and atypical protein kinase C isoforms in myocytes (5). Interestingly, the possible involvement of AMPK-independent signaling has been also proposed, using the system of overexpression of a dominant negative AMPK mutant (26). It should be an interesting issue to be resolved, therefore, how AMPK-dependent and -independent pathways are related to the AICAR-induced glucose uptake observed in 3T3-L1 adipocytes. On the other hand, in adipose cells including 3T3-L1, it has been observed that GLUT1, another isoform of glucose transporters, is also functionally expressed (12). AICAR has been reported to increase the intrinsic activity of GLUT1 protein via activated p38 MAPK to enhance the glucose transport into Clone 9 cells, a rat liver-derived, non-transformed cell line that expresses only the GLUT1 (1, 31). The increased intrinsic activity of GLUT1 as well as GLUT4 could potentially induce the enhancement of glucose uptake after AMPK activation in 3T3-L1 adipocytes. In contrast to our findings, Salt et al. (27) have demonstrated that AICAR does not significantly enhance the translocation of GLUT4 or GLUT1 to the plasma membrane, whereas a modest stimulation of glucose uptake was simultaneously observed. The precise reason for the discrepancy in the translocation of GLUT4 between their results and ours is still unclear at present, but the effect on 3T3-L1 cells might have been too small in their experiments to be detected by the plasma membrane lawn assay, because their method is supposedly less sensitive for the detection compared with ours using the system of the GLUT$_{4-e}$ GFP chimeric protein. Further studies concerning the intracellular system for translocation and activation of various GLUT isoforms are necessary to clarify this issue.

In the present study, it is revealed that AMPK activators AICAR and DNP can accelerate GLUT4 translocation in 3T3-L1 adipocytes, as has been observed in skeletal muscles. The mode of action on the translocation through AMPK activation was as quick, within 4 min, as in the case of insulin stimulation, but it was shown to be mediated by a signaling system distal to the PI3K activation through insulin stimulation or by a pathway distinct from that activated by insulin. On the other hand, the enhancement of glucose uptake was further mediated by the increased intrinsic activity of GLUT4 protein, possibly through p38 MAPK activation. The activation of AMPK in adipocytes would be a new therapeutic target for the glycemic control of type 2 diabetes.

### REFERENCES

1. Abbud W, Habinowski S, Zhang JZ, Kendrew J, Elkairi FS, Kemp BE, Witters LA, and Ismail-Beigi F. Stimulation of AMP-activated protein kinase (AMPK) is associated with enhancement of GLUT1-mediated glucose transport. Arch Biochem Biophys 380: 347–352, 2000.

2. **Barros LF, Barnes K, Ingram JC, Castro J, Porras OH, and Baldwin SA.** Hyperosmotic shock induces both activation and translocation of glucose transporters in mammalian cells. *Pflügers Arch* 442: 614–621, 2001.

3. **Bazuine M, Ouwens DM, Gomes de Mesquita DS, and Massen JA.** Arsenite stimulated glucose transport in 3T3-L1 adipocytes involves both Glut4 translocation and p38 MAPK activity. *Eur J Biochem* 270: 3891–3903, 2003.

4. **Chen D, Elmendorf JS, Olson AL, Li X, Earp HS, and Pessin JE.** Osmotic shock stimulates GLUT4 translocation in 3T3-L1 adipocytes by a novel tyrosine kinase pathway. *J Biol Chem* 272: 27401–27410, 1997.

5. **Chen HC, Bandyopadhyay G, Sajan MP, Kanoh Y, Standaert M, Farese RV Jr, and Farese RV.** Activation of the ERK pathway and atypical protein kinase C isoforms in exercise- and aminoimidazole-4-carboxamide-1-β-D-riboside (AICAR)-stimulated glucose transport. *J Biol Chem* 277: 23554–23562, 2002.

6. **Corton JM, Gillespie JG, Hawley SA, and Hardie DG.** 5-Aminoimidazole-4-carboxamide ribonucleoside: a specific method for activating AMP-activated protein kinase in intact cell? *Eur J Biochem* 229: 558–565, 1995.

7. **Frevert EU and Kahn BB.** Differential effects of constitutively active phosphatidylinositol 3-kinase on glucose transport, glycogen synthase activity and DNA synthesis in 3T3-L1 adipocytes. *Mol Cell Biol* 17: 190–198, 1997.

8. **Fryer LG, Parbu-Patel A, and Carling D.** Protein kinase inhibitors block the stimulation of the AMP-activated protein kinase by 5-amino-4-imidazolecarboxamide riboside. *FEBS Lett* 531: 189–192, 2002.

9. **Hardie DG and Carling D.** The AMP-activated protein kinase: fuel gauge of the mammalian cell? *Eur J Biochem* 246: 259–273, 1997.

10. **Hayashi T, Hirshman MF, Kurth EJ, Winder WW, and Goodyear LJ.** Evidence of 5′ AMP-activated protein kinase mediation of the effect of muscle contraction on glucose transport. *Diabetes* 47: 1369–1373, 1998.

11. **Ihlemann J, Ploug T, Hellsten Y, and Galbo H.** Effect of tension on contraction-induced glucose transport in rat skeletal muscle. *Am J Physiol Endocrinol Metab* 277: E208–E214, 1999.

12. **Kaestner KH, Chirsty RJ, McLenithan JC, Braiterman LT, Cornelius P, Pekala PH, and Lane MD.** Sequence, tissue distribution, and differential expression of mRNA for a putative insulin-responsive glucose transporter in mouse 3T3-L1 adipocytes. *Proc Natl Acad Sci USA* 86: 3150–3154, 1989.

13. **Kanai F, Ito K, Todaka M, Hayashi H, Kamohara S, Ishii K, Okada T, Hazeki O, Ui M, and Ebina Y.** Insulin-stimulated GLUT4 translocation is relevant to the phosphorylation of IRS-1 and the activity of PI3-kinase. *Biochem Biophys Res Commun* 195: 762–768, 1993.

14. **Katagiri H, Asano T, Ishihara H, Inukai K, Shibasaki Y, Kikuchi M, Yazaki Y, and Oka Y.** Overexpression of catalytic subunit p110α of phosphatidylinositol 3-kinase increases glucose transport activity with translocation of glucose transporters in 3T3-L1 adipocytes. *J Biol Chem* 271: 16987–16990, 1996.

15. **Kishi K, Muromoto N, Nakaya Y, Miyata I, Hagi A, Hayashi H, and Ebina Y.** Bradykinin directly triggers GLUT4 translocation via an insulin-independent pathway. *Diabetes* 47: 550–558, 1998.

16. **Kotani K, Carozzi AJ, Sakaue H, Hara K, Robinson LJ, Clark SF, Yonezawa K, James DE, and Kasuga M.** Requirement for phosphoinositide 3-kinase in insulin-stimulated GLUT4 translocation in 3T3-L1 adipocytes. *Biochem Biophys Res Commun* 209: 343–348, 1995.

17. **Kurth-Kraczek EJ, Hirshman MF, Goodyear LJ, and Winder WW.** 5′AMP-activated protein kinase activation causes GLUT4 translocation in skeletal muscle. *Diabetes* 48: 1667–1671, 1999.

18. **Lemieux K, Konrad D, Klip A, and Marette A.** The AMP-activated protein kinase activator AICAR dose not induce GLUT4 translocation to transverse tubules but stimulates glucose uptake and p38 mitogen-activated protein kinases α and β in skeletal muscle. *FASEB J* 17: 1658–1665, 2003.

19. **Merrill GF, Kurth EJ, Hardie DG, and Winder WW.** AICA riboside increases AMP-activated protein kinase, fatty acid oxidation, and glucose uptake in rat muscle. *Am J Physiol Endocrinol Metab* 273: E1107–E1112, 1997.

20. **Mu J, Brozinick JT, Valladares O, Bucan M, and Birnbaum MJ.** A role for AMP-activated protein kinase in contraction- and hypoxia-regulated glucose transport in skeletal muscle. *Mol Cell* 7: 1085–1094, 2001.

21. **Nakamichi Y, Ohara-imaizumi M, Ishida H, and Nagamatsu S.** An insulin-related peptide expressed in 3T3-L1 adipocytes is localized in GLUT4 vesicles and secreted in response to exogenous insulin, which augments the insulin-stimulated glucose uptake. *J Cell Sci* 116: 73–79, 2003.

22. **Oatey PB, Van Weering DHJ, Dobson SP, Gould GW, and Tavaré JM.** GLUT4 vesicle dynamics in 3T3-L1 adipocytes visualized with green-fluorescent protein. *Biochem J* 327: 637–642, 1997.

23. **Patki V, Buxton J, Chawla A, Lifshitz L, Fogarty K, Carrington W, Tuft R, and Corvera S.** Insulin action on GLUT4 traffic visualized in single 3T3-L1 adipocytes by using ultra-fast microscopy. *Mol Biol Cell* 12: 129–141, 2001.

24. **Pessin JE, Thurmond DC, Elmendorf JS, Coker KJ, and Okada S.** Molecular basis of insulin-stimulated GLUT4 vesicle trafficking. *J Biol Chem* 274: 2593–2596, 1999.

25. **Powell KA, Campbell LC, Tavaré JM, Leader DP, Wakefield JA, and Gould GW.** Trafficking of GLUT4-green fluorescent protein chimaeras in 3T3-L1 adipocytes suggests distinct internalization mechanisms regulating cell surface GLUT4 levels. *Biochem J* 344: 535–543, 1999.

26. **Sakoda H, Ogihara T, Anai M, Fujishiro M, Ono H, Onishi Y, Katagiri H, Abe M, Fukushima Y, Shojima N, Inukai K, Kikuchi M, Oka Y, and Asano T.** Activation of AMPK is essential for AICAR-induced glucose uptake by skeletal muscle but not adipocytes. *Am J Physiol Endocrinol Metab* 282: E1239–E1244, 2002.

27. **Salt IP, Connell JMC, and Gould GW.** 5-Aminoimidazole-4-carboxamide ribonucleoside (AICAR) inhibits insulin-stimulated glucose transport in 3T3-L1 adipocytes. *Diabetes* 49: 1649–1656, 2000.

28. **Somwar R, Niu W, Kim DY, Sweeney G, Randhara VK, Huang C, Ramlal T, and Klip A.** Differential effects of phosphatidylinositol 3-kinase inhibition on intracellular signals regulating GLUT4 translocation and glucose transport. *J Biol Chem* 276: 46079–46087, 2001.

29. **Somwar R, Koterski S, Sweeney G, Sciotti R, Djuric S, Berg C, Trevillyan J, Scherer PE, Rondinone CM, and Klip A.** A dominant-negative p38 MAPK mutant and novel selective inhibitors of p38 MAPK reduce insulin-stimulated glucose uptake in 3T3-L1 adipocytes without affecting GLUT4 translocation. *J Biol Chem* 277: 50386–50395, 2002.

30. **Winder WW and Hardie DG.** AMP-activated protein kinase, a metabolic master switch: possible roles in type 2 diabetes. *Am J Physiol Endocrinol Metab* 277: E1–E10, 1999.

31. **Xi X, Han J, and Zhang JZ.** Stimulation of glucose transport by AMP-activated protein kinase via activation of p38 mitogen-activated protein kinase. *J Biol Chem* 276: 41029–41034, 2001.

# ELKS, a Protein Structurally Related to the Active Zone-associated Protein CAST, Is Expressed in Pancreatic β Cells and Functions in Insulin Exocytosis: Interaction of ELKS with Exocytotic Machinery Analyzed by Total Internal Reflection Fluorescence Microscopy<span>[V]</span>

Mica Ohara-Imaizumi,* Toshihisa Ohtsuka,[†‡] Satsuki Matsushima,[§]
Yoshihiro Akimoto,[||] Chiyono Nishiwaki,* Yoko Nakamichi,* Toshiteru Kikuta,*
Shintaro Nagai,* Hayato Kawakami,[||] Takashi Watanabe,[§] and Shinya Nagamatsu*

Departments of *Biochemistry, [§]Clinical Pathology, and [||]Anatomy, Kyorin University School of Medicine,
Mitaka, Tokyo 181-8611, Japan; and [†]KAN Research Institute, Shimogyo-ku, Kyoto 600-8815, Japan

The cytomatrix at the active zone (CAZ) has been implicated in defining the site of $Ca^{2+}$-dependent exocytosis of neurotransmitters. Here, we demonstrate the expression and function of ELKS, a protein structurally related to the CAZ protein CAST, in insulin exocytosis. The results of confocal and immunoelectron microscopic analysis showed that ELKS is present in pancreatic β cells and is localized close to insulin granules docked on the plasma membrane-facing blood vessels. Total internal reflection fluorescence microscopy imaging in insulin-producing clonal cells revealed that the ELKS clusters are less dense and unevenly distributed than syntaxin 1 clusters, which are enriched in the plasma membrane. Most of the ELKS clusters were on the docking sites of insulin granules that were colocalized with syntaxin 1 clusters. Total internal reflection fluorescence images of single-granule motion showed that the fusion events of insulin granules mostly occurred on the ELKS cluster, where repeated fusion was sometimes observed. When the Bassoon-binding region of ELKS was introduced into the cells, the docking and fusion of insulin granules were markedly reduced. Moreover, attenuation of ELKS expression by small interfering RNA reduced the glucose-evoked insulin release. These data suggest that the CAZ-related protein ELKS functions in insulin exocytosis from pancreatic β cells.

## INTRODUCTION

The release of neurotransmitters is restricted to specialized presynaptic membrane compartments called active zones (Landis et al., 1988). The cytomatrix at the active zone (CAZ) is thought to play an organizational role in defining presyn-

Abbreviations used: BSA, bovine serum albumin; CAZ, cytomatrix at the active zone; CCD, charge-coupled device; EPIF, epifluorescence; GFP, green fluorescent protein; KRB, Krebs-Ringer buffer; mAb, monoclonal antibody; pAb, polyclonal antibody; PBS, phosphate-buffered saline; PSF, point spread function; PTD, protein transduction domain; SNAP-25, synaptosomal associated protein of 25 kDa; TIRFM, total internal reflection fluorescence microscopy; t-SNARE, target-soluble N-ethylmaleimide–sensitive factor attachment protein receptor.

aptic sites of synaptic vesicle docking and fusion (Garner et al., 2000). On the other hand, the fusion of vesicles is mediated by the formation of the soluble N-ethylmaleimide–sensitive factor attachment protein receptor (SNARE) complex of the presynaptic plasma membrane protein syntaxin 1 and synaptosomal associated protein of 25 kDa (SNAP-25) and the synaptic vesicle protein vesicle-associated membrane protein-2 (Rizo and Südhof, 2002). Although the role of CAZ is understood in neurons, the role of active zones or exocytotic "hot spots" is still unclear in other regulated secretory cells, including pancreatic β cells, where the SNARE complex also plays an important role in their exocytotic processes (Daniel et al., 1999; Nagamatsu et al., 1999).

Recently, several CAZ-related specific proteins in neurons, including Bassoon, RIMs, Munc13s, Piccolo/Aczonin, and CASTs, have been identified and are thought to have a function in synaptic vesicle exocytosis and in the spatial organization of transmitter release (Gundelfinger et al., 2003; Rosenmund et al., 2003). RIM1, a small G protein Rab3A effector, regulates the $Ca^{2+}$-dependent exocytosis of neurotransmitters in a Rab3A-dependent manner (Wang et al., 1997; Castillo et al., 2002; Schoch et al., 2002). Munc13-1 binds both RIM1 and the target (t)-SNARE syntaxin 1 and is implicated in the priming of synaptic vesicles (Brose et al., 2000; Betz et al., 2001). Bassoon and Piccolo/Aczonin are very large (>400 kDa) and are structurally related CAZ proteins (tom Dieck et al., 1998; Wang et al., 1999). Genetic knockout

studies in several organisms have confirmed the importance of RIM1, Munc13-1, and Bassoon in synaptic vesicle exocytosis; disruption of RIM1 and Munc13-1 genes reduced the neurotransmitter release (Martin, 2002; Rosenmund et al., 2002; Schoch et al., 2002; Gundelfinger et al., 2003), and the loss of Bassoon resulted in impaired synaptic transmission and ectopic synapse formation in mouse retina (Altrock et al., 2003; Dick et al., 2003). In addition, CAST directly binds Bassoon, Piccolo, and RIM1 and indirectly binds Munc13-1 through RIM1, which suggests that CAST may act as a platform for form action of a dynamic multicomplex at the CAZ (Ohtsuka et al., 2002; Takao-Rikitsu et al., 2004). On the other hand, the t-SNAREs syntaxin1 and SNAP-25 are not specifically localized to active zones, but rather they are present on the entire axonal plasma membrane (Garcia et al., 1995). Given the spatial restriction of synaptic transmitter release to CAZ, the CAZ complex must exist at active zones that regulate SNARE function and thus cause the spatial restriction of the fusion process (Rosenmund et al., 2003). Thus, CAZ multicomplexing through CAST might be physically and functionally associated with the SNARE complex and regulate neurotransmitter release (Takao-Rikitsu et al., 2004).

Recently, Fujimoto et al. (2002) reported that several CAZ proteins identified in neurons also were expressed in pancreatic $\beta$ cells, as found by using reverse transcription (RT)-PCR analysis, with the exception of CAST (Fujimoto et al., 2002); however, detailed localization and the functional roles of these proteins in insulin exocytosis are not known. To clarify the functions of the CAZ protein in insulin exocytosis that must function in collaboration with the SNAREs, we first examined the expression and localization of ELKS (Nakata et al., 1999), a protein structurally related to CAST (Deguchi-Tawarada et al., 2004) in pancreatic $\beta$ cells. ELKS was first identified as a gene with a 5' terminus fused to the RET tyrosine kinase oncogene in a papillary thyroid carcinoma (Nakata et al., 1999). Recently, ELKS also has been identified as Rab6-interacting protein 2 (Monier et al., 2002), ERC1 (Wang et al., 2002), and CAST2 (Deguchi-Tawarada et al., 2004), and its functions have been studied; ELKS seems to be involved in intracellular membrane traffic in several tissues (Monier et al., 2002; Wang et al., 2002), and, notably, ELKS is a component of active zones in the brain that binds RIMs (Wang et al., 2002; Deguchi-Tawarada et al., 2004). So far, there is no report showing the expression and function of ELKS in pancreatic $\beta$ cells. In this study, we found that ELKS was appreciably expressed in rat pancreatic islets and in an insulin-producing clonal cell line, MIN6 $\beta$ cells, where ELKS was colocalized with both insulin granules and syntaxin 1. We then investigated how ELKS functions in the docking and fusion of insulin granules by using living MIN6 $\beta$ cells and total internal reflection fluorescence (TIRF) image analysis. The data obtained indicate that ELKS is involved in the regulation of insulin exocytosis.

## MATERIALS AND METHODS

### Plasmids

The construction of green fluorescent protein (GFP)-insulin expression vector has been described previously (Ohara-Imaizumi et al., 2004b). To produce constructs in which the TAT protein transduction domain (PTD) peptide is located at the N terminus of either the ELKS Bassoon-binding domain (ELKS-BsnBD, aa 405–602) or the ELKS noncoiled-coil control domain (ELKSContD, aa 324–403), the coding region that corresponds to mouse ELKSBsnBD or ELKSContD was amplified by PCR by using oligonucleotide primers including the nucleotide sequence against the TAT PTD peptide (YGRKKRRQRRR) in each sense primer, as described previously (Ohara-Imaizumi et al., 2002a), and the PCR products were subcloned into a pPROEX vector with or without

an Myc-tag. The resulting products were confirmed by an automated DNA sequencer (Amersham Biosciences UK, Little Chalfont, Buckinghamshire, United Kingdom).

### Antibodies (Abs)

Polyclonal (p) anti-CAST (anti-CAST pAb; Takao-Rikitsu et al., 2004) and anti-ELKS (anti-ELKS pAb; Deguchi-Tawarada et al., 2004) were used. A mouse monoclonal antibody (mAb) against ELKS (anti-ELKS mAb) was raised against a peptide corresponding to aa 117–142, according to standard methods. Mouse monoclonal anti-Bassoon (StressGen Biotechnologies, Victoria, Ontario, Canada), mouse monoclonal anti-Munc13-1 (Synaptic Systems, Goettingen, Germany), mouse monoclonal anti-syntaxin 1 (Sigma-Aldrich, St. Louis, MO), mouse monoclonal anti-insulin (Sigma-Aldrich), mouse monoclonal anti-vascular endothelial (VE)-cadherin (BD Biosciences, San Jose, CA), mouse monoclonal anti-c-Myc (9E10) (Chemicon International, Temecula, CA), mouse monoclonal anti-GFP (Roche Diagnostics, Basel, Switzerland), mouse monoclonal anti-HA (Roche Diagnostics, Indianapolis, IN), rabbit polyclonal anti-RIM2 (Synaptic Systems), and guinea pig anti-insulin (Dako-Cytomation Denmark A/S, Glostrup, Denmark) antibodies were purchased from commercial sources.

### Cell Culture and Transfection

MIN6 cells (a gift from Dr. J.-I. Miyazaki, Osaka University, Osaka, Japan) at passage 15–30 were cultured as described previously (Nagamatsu et al., 1999) on fibronectin-coated (KOKEN, Tokyo, Japan) high-refractive index glass (Olympus, Tokyo, Japan) for imaging by TIRF microscopy or on glass chamber slides (eight wells, Lab-Tek slides; Nunc, Rochester, NY). MIN6 cells were transfected with the expression vector encoding the GFP-tagged insulin as described previously (Ohara-Imaizumi et al., 2002b). All experiments were performed within 3 d after transfection.

### Immunofluorescence Staining

Immunofluorescence staining of rat pancreas was performed as described previously with minor modification (Nagamatsu et al., 1996). In brief, rat pancreas was dissected in 4% paraformaldehyde in 0.1 M phosphate buffer, pH 7.4, cryoprotected with graded concentrations of sucrose in phosphate-buffered saline (PBS), embedded in OCT compound (Miles, Elkhart, IN), and then frozen by immersion in liquid nitrogen. Semithin frozen sections were cut with a Miles cryostat, transferred to poly-L-lysine–coated thin slides (0.1 mm in thickness; Matsunami Glass, Osaka, Japan), and immunostained. Sections were incubated with primary antibodies (rabbit anti-ELKS pAb, mouse anti-insulin mAb, and mouse anti-VE-cadherin antibody, diluted 1:200) in PBS containing 4% fetal calf serum, 0.1% sodium azide, and 0.25% Triton X-100, followed by secondary antibodies (goat anti-mouse IgG conjugated to Texas Red (Molecular Probes, Eugene, OR) or goat anti-rabbit IgG conjugated to fluorescein (Sigma-Aldrich). The sections were examined by using laser-scanning confocal microscopy (optical slice of 1 $\mu$m: LSM510 with Zeiss 10 and 100× Plan-Neofluar objective; Carl Zeiss, Oberkochen, Germany).

For immunostaining, MIN6 $\beta$ cells were fixed with ice-cold 100% methanol for 20 s and were permeabilized with 0.25% Triton X-100. Cells were incubated with the primary antibodies in PBS containing 3% bovine serum albumin (BSA) (Sigma-Aldrich) and 0.25% Triton X-100 for 2 h at room temperature, followed by the addition of secondary antibodies (goat anti-mouse IgG conjugated to Alexa Fluor-488, -546, and -633 (Molecular Probes), goat anti-rabbit IgG conjugated to Alexa Fluor-488 and -546 (Molecular Probes), or goat anti-guinea pig IgG conjugated to fluorescein (Sigma-Aldrich) for 1 h at room temperature.

### Immunogold Labeling for Electron Microscopy

Immunogold labeling was carried out as described previously (Akimoto et al., 1999). The pancreas was fixed in 4% paraformaldehyde phosphate-buffered saline at 4°C for 2 h. After having been washed with PBS, specimens were dehydrated through a series of graded ethanols and were embedded in LR White resin (London Resin, Basingstoke, United Kingdom). Ultrathin sections were cut and mounted on nickel grids. The sections were incubated with 5% normal donkey serum phosphate-buffered saline for 1 h and they were incubated with anti-ELKS pAb antibody at 4°C for 24 h. As cytochemical controls, nonimmunized rabbit IgG was incubated with samples. After washing with PBS, the samples were incubated with 12-nm colloidal gold-conjugated donkey anti-rabbit IgG antibody (Jackson ImmunoResearch Laboratories, West Grove, PA) at room temperature for 2 h. After another wash with PBS, they were incubated with anti-insulin mAb (Sigma-Aldrich) at 4°C for 24 h. As cytochemical controls, nonimmunized mouse IgG was incubated with samples. After washing with PBS, the samples were incubated with 18-nm colloidal gold-conjugated donkey anti-mouse IgG antibody (Jackson ImmunoResearch Laboratories) at room temperature for 2 h. The specimen were washed with PBS and then fixed in 2% glutaraldehyde. After rinsing with deionized water, ultrathin sections were stained with uranyl acetate and were observed with a transmission electron microscope (JEM-1010; JEOL, Tokyo, Japan).

## TAT-conjugated Antibody

TAT-conjugated Cy3-labeled anti-ELKS antibody was prepared as described previously (Ohara-Imaizumi *et al.*, 2004a). In brief, anti-ELKS mAb was labeled with Cy3 by use of a Fluoro Link-antibody Cy3 labeling kit (Amersham Biosciences UK), according to manufacture's instructions. The Cy3-labeled antibody was dialyzed against 0.1 M borate buffer and was incubated with a fivefold molar excess of a cross-linker, sulfosuccinimidyl 6-[3'-(2-pyridyldithio)-propionamido] hexanoate (Pierce Chemical, Rockford, IL) for 3 h at room temperature. The conjugated antibody was separated from free cross-linker by gel filtration eluted with HBSS-HEPES (5 mM) buffer, pH 7.2. A 10-fold molar excess of TAT PTD peptide (GYGRKKRRQRRRGGGC) was added to the conjugated antibody, and the mixture was incubated overnight at 4°C. The TAT-conjugated antibody was separated from free TAT PTD peptide by gel filtration eluted with HBSS-HEPES (5 mM) buffer. On the day of experiments using TIRFM, MIN6 cells were transduced for 40 min with the TAT-conjugated Cy3-labeled anti-ELKS mAb (~120 µg/ml).

## TIRFM

The Olympus TIRF system was used with an inverted microscope (IX70; Olympus) and a high-aperture objective lens (Apo 100× OHR; numerical aperture 1.65; Olympus) as described previously (Ohara-Imaizumi *et al.*, 2002b). In this study, the microscope was modified to allow both epifluorescence (EPIF) and through-the-objective TIRF illumination. To observe GFP alone, we used a 488-nm laser line for excitation and a 515-nm long-pass filter for the barrier. To observe the fluorescence image of GFP and Cy3 simultaneously under TIRF illumination, we used the 488-nm laser line for excitation and an image splitter (MultiSpec MicroImager; Optical Insight, Santa Fe, NM) that divided the green and red components of the images with 565-nm dichroic mirror (Q565; Chroma Technology, Brattleboro, VT) and passed the green component through a 530 ± 15-nm bandpass filter (HQ530/30m; Chroma Technology) and the red component through a 630 ± 25-nm bandpass filter (HQ630/50m; Chroma Technology). The images were then projected side by side onto a cooled charge-coupled device (CCD) camera (DV887DCSBV; ANDOR Technology, Belfast, Northern Ireland; operated with MetaMorph version 6.2; Universal Imaging, Downingtown, PA). Images were acquired at 300-ms intervals. Most analyses, including tracking (single projection of difference images) and area calculations, were performed using MetaMorph software. The two images were brought into focus in the same plane by adding weak lenses to one channel, and they were brought into resister by careful adjustment of the mirrors in the image splitter. Before each experimental session, we took an alignment image that showed density by means of scattered 90-nm TetraSpeck fluorescent beads (Molecular Probes). They were visible in both the green and red channels and thus provided markers in the x-y plane. Beads in the two images were brought into superposition by shifting one image by using MetaMorph software. The space constant for the exponential decay of the evanescent field was ~43 nm. For the study of the real-time images of GFP-tagged insulin granule motion by TIRF, treated MIN6 cells were placed on the high refractive index glass, mounted in an open chamber, and incubated for 30 min at 37°C in Krebs-Ringer buffer (KRB) containing 110 mM NaCl, 4.4 mM KCl, 1.45 mM KH$_2$PO$_4$, 1.2 mM MgSO$_4$, 2.3 mM calcium gluconate, 4.8 mM NaHCO$_3$, 2.2 mM glucose, 10 mM HEPES, pH 7.4, and 0.3% BSA. Cells were then transferred to the thermostat-controlled stage (37°C) of TIRFM. Stimulation with KCl was achieved by the addition of 100 mM KCl-KRB (NaCl was reduced to maintain the isotonicity of the solution) into the chamber (final concentration, 50 mM KCl). On the day of experiments using TIRFM, MIN6 cells were transduced for 50 min with 70 µg/ml TAT fusion proteins.

To observe the TIRF image from triple immunostaining of MIN6 cells, we used the TIRFM with an arc-lamp source (IX2-ARCEVA; Olympus). To observe fluorescein, a filter of 490 ± 10 was used for excitation, and the emission signals were filtered with 528 ± 19-nm band-pass filter. To observe Alexa Fluor-546, a filter of 555 ± 14 was used for excitation, and the emission signals were filtered with 617 ± 36-nm band-pass filter. To observe Alexa Fluor 633, a filter of 635 ± 10 was used for excitation, and the emission signals were filtered with 685 ± 20-nm band-pass filter. Images were collected by the cooled CCD camera operated with MetaMorph software and then were analyzed by MetaMorph.

## Insulin Release Assay

Control and TAT fusion protein-treated (70 µg/ml for 50 min) MIN6 cells were housed in a small chamber and perifused with the KRB (2.2 mM glucose) for 60 min at a flow rate of 0.5 ml/min at 37°C before the collection of fractions. Insulin release was stimulated by 22 mM glucose. Fractions were collected at 1-min intervals. At the end of the stimulation period, the cells were disrupted by sonication, and aliquots of media and cell extracts were analyzed for immunoreactive insulin (IRI) by radioimmunoassay. The amount of released insulin is expressed as a percentage of the total cellular content per minute.

## Measurement of $[Ca^{2+}]_i$

MIN6 cells were loaded with 10 µM fura-2 acetoxymethyl ester (Fura-2 AM, Molecular Probes) for 30 min at 37°C in KRB (2.2 mM glucose), followed by washing and an additional 15-min incubation with KRB. Then, the coverslips were mounted on an ARGUS/HiSCA system (Hamamatsu Photonics, Hamamatsu, Japan). Fura-2 fluorescence was detected by cooled CCD camera after excitation at wavelengths of 340 nm (F340) and 380 nm (F380), and the ratio image (F340/F380) was calculated by use of the ARGUS/HiSCA system.

## Immunoblotting

Proteins were extracted from rat brain or MIN6 cells by homogenization, or from rat islets, with the 1% Triton X-100 lysis buffer, and then were boiled in SDS sample buffer with 10 mM dithiothreitol subjected to SDS-PAGE, and then transferred onto nitrocellulose filters. The filter was incubated with anti-CAST or anti-ELKS pAbs followed by horseradish peroxidase-conjugated secondary antibody, and the bands were visualized by use of a chemiluminescence detection system (PerkinElmer Life and Analytical Sciences, Boston, MA).

## Immunoprecipitation

For the in vitro binding studies of ternary complex formation of ELKS, Bassoon, and RIM2, immunoprecipitation was performed as described previously (Ohtsuka *et al.*, 2002). In brief, each expression plasmid of Myc-ELKS, enhanced green fluorescent protein (EGFP)-Bassoon, or HA-RIM2 was transfected into human embryonic kidney (HEK)293 cells, and each protein was extracted and mixed. After incubation overnight at 4°C, immunoprecipitation was performed using anti-GFP antibody. The samples were then analyzed by immunoblotting. To examine the effects of TAT-ELKSBsnBD on the binding of ELKS and Bassoon, an immunoprecipitation assay for Myc-ELKS and EGFP-Bassoon was performed in the presence or absence of Myc-tagged TAT-ELKSBsnBD by using anti-GFP antibody, as described previously (Takao-Rikitsu *et al.*, 2004). In brief, each expression plasmid of Myc-ELKS and EGFP-Bassoon was transfected into HEK293 cells, and each protein was extracted and mixed in the presence or absence of Myc-tagged TAT-ELKSBsnBD. After incubation overnight at 4°C, immunoprecipitation was performed using anti-GFP antibody. The samples were then analyzed by immunoblotting by using anti-Myc and anti-GFP antibodies.

For immunoprecipitation from MIN6 cells, the MIN6 cell lysates were immunoprecipitated with anti-Bassoon mAb or anti-Myc mAb (as a control) and pelleted with protein A-Sepharose (Nagamatsu *et al.*, 1996). The immunoprecipitates were subjected to immunoblot analysis with anti-Bassoon mAb, anti-ELKS pAb, and anti-RIM2 pAb.

## Pull-Down Assay

Myc-tagged TAT-ELKSBsnBD was incubated with glutathione-Sepharose beads containing GST-Bassoon and GST-Piccolo at 4°C overnight as described previously (Ohtsuka *et al.*, 2002). After the beads were extensively washed with the lysis buffer, the bound proteins were eluted by boiling the beads in an SDS sample buffer [60 mM Tris-HCl, pH 6.7, 3% SDS, 2% (vol/vol) 2-mercaptoethanol, and 5% glycerol] for 5 min. The samples were then analyzed by immunoblotting by using the anti-Myc antibody.

## ELKS RNA Interference

The following 21-mer oligonucleotide pairs were used as small interfering RNA (siRNA) against mouse ELKS: 5'-r(CAGUGUUGGAGGUGGCAGU) d(TT)-3' and 5'-r(ACUGCCACCUCCAACACUG)d(TT)-3' (synthesized by QIAGEN, Valencia, CA). A GFP-22 siRNA (QIAGEN) was used as a nonspecific control. The ELKS siRNA and GFP-22 siRNA were transfected into MIN6 cells by using RNAiFect (QIAGEN) according to the manufacturer's protocol. The efficiency and specificity of the siRNA targeted against ELKS were assessed by cotransfection of expression vector encoding Myc-tagged ELKS and siRNA-ELKS into HEK293 cells (Figure 13A).

## Point Spread Function (PSF)

To obtain the estimation of real diameter of the clusters in the TIRF images, the PSF was determined by measuring the diameter of 90-nm fluorescent beads (Molecular Probes), which was 340 ± 27 nm (35 beads) under our experimental conditions: $PSF = [(beads_{measured\ diameter})^2 - (beads_{real\ diameter})^2]^{1/2}$. The real diameter of the spots was calculated by subtraction of the PSF: $[cluster_{real\ size} = [(cluster_{measured\ size})^2 - (PSF)^2]^{1/2}]$ as described previously (Ohara-Imaizumi *et al.*, 2004a).

## RESULTS

### ELKS Is Abundantly Present in Pancreatic Islet

First, we studied the expression of CAST and ELKS protein in rat pancreatic islets, by using immunoblot analysis. Figure 1A shows that rat islets expressed ELKS but not CAST protein, whereas rat brain (used as positive control) expressed both CAST and ELKS proteins. The ELKS protein in islets exhibited distinct gel mobility, compared with that in

**A**



**B**



**C**
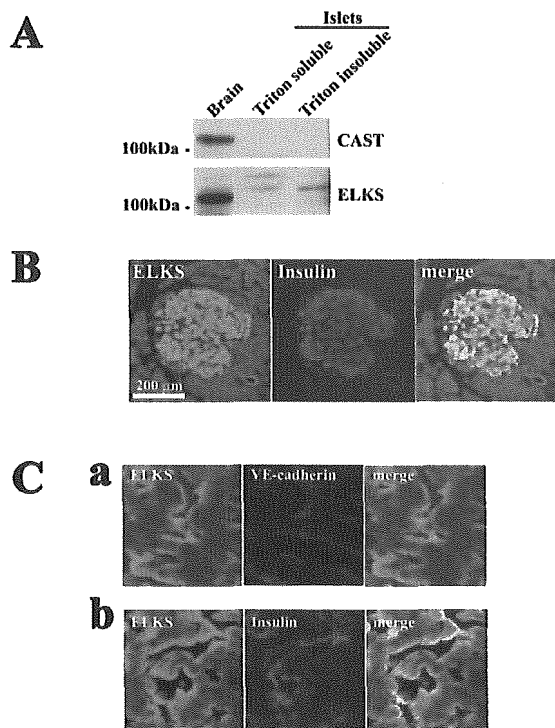


**Figure 1.** ELKS is present in pancreatic islet $\beta$ cells. (A) Immunoblot analysis of the pancreatic islet lysate by using anti-CAST and anti-ELKS antibodies. Rat brain homogenate (used as positive control) and rat pancreatic islet lysate (1% Triton X-100–soluble and –insoluble fractions) (20 $\mu$g of each protein) were analyzed by immunoblotting by using anti-CAST or anti-ELKS pAbs. Note that rat islets expressed ELKS but not CAST, whereas rat brain expressed both CAST and ELKS. (B) Colocalization of ELKS and insulin in rat pancreatic islets as determined by immunofluorescence labeling and confocal laser microscopy. Islets were immunostained for ELKS and insulin and were viewed in the green (ELKS) or the red (insulin) channel. There was significant overlap (merged [yellow]) of ELKS and insulin immunofluorescence. Magnification, 10×; bars, 200 $\mu$m. (C) Localization of ELKS, insulin, and VE-cadherin in islets by immunofluorescence labeling and confocal laser microscopy with higher magnification (100×). Islets were double stained using anti-ELKS pAb and anti-VE-cadherin mAb (a) or anti-insulin mAb (b). Bars, 20 $\mu$m.

the brain. It has been reported that the anti-ELKS pAb recognized a protein band of 120 kDa in rat brain and multiple protein bands of ~130–140 kDa in other rat tissues, including the spleen, lung, liver, muscle, kidney, and testis. The data suggest that there are multiple splice variants of ELKS (i.e., ELKS$\alpha$ and the other ELKS isoforms) in tissues other than the brain (Yokota *et al.*, 2000; Monier *et al.*, 2002; Wang *et al.*, 2002; Deguchi-Tawarada *et al.*, 2004). Therefore, the protein bands of ~130–140 kDa observed in islets seemed to be due to $\beta$ cell-specific splice variants of ELKS.

Because ELKS is a major protein with CAST family that is expressed in pancreatic islets, we then examined the localization of ELKS in rat pancreatic islets, by immunohistochemistry by using confocal laser microscopy. As shown in Figure 1B, ELKS immunostaining was mainly observed in the pancreatic islets. Double staining for insulin and ELKS showed that the immunoreactivity of ELKS was seen in insulin-positive $\beta$ cells, which indicates that ELKS is most abundant in $\beta$ cells. The immunofluorescence of the other
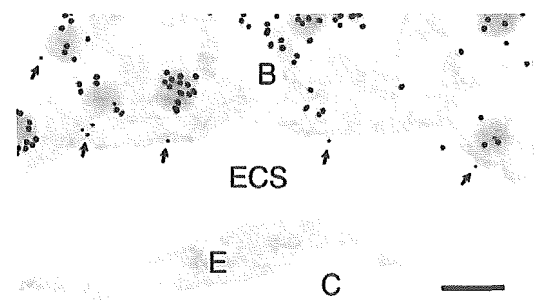


**Figure 2.** Ultrastructural localization of ELKS in $\beta$ cells. Ultrathin sections of the rat pancreas were reacted with the anti-ELKS pAb, and then with 12-nm colloidal gold-conjugated donkey anti-rabbit IgG antibody. Next, they were incubated with anti-insulin mAb and then with 18-nm colloidal gold-conjugated donkey anti-mouse IgG antibody. Note that the immunoreactivity of ELKS (small gold particles) was frequently detected close to insulin-containing granules (large gold particles) docked on the plasma membrane facing blood capillary (arrows). B, $\beta$ cell; C, blood capillary; E, endothelial cell; ECS, extracellular space. Bar, 0.2 $\mu$m.

CAZ proteins, Bassoon, RIM2, and Munc13-1, also was detected in pancreatic islets, but CAST immunofluorescence was not detectable (our unpublished data), which is consistent with the results as shown in Figure 1A and those of a previous report of assessment by RT-PCR analysis (Fujimoto *et al.*, 2002).

The confocal imaging of islets by higher magnification (100×) showed that ELKS was localized at the plasmalemmal region of rat pancreatic $\beta$ cells, especially those facing blood capillaries labeled with VE-cadherin, a marker for endothelial cells (Lampugnani *et al.*, 1992; Vasir *et al.*, 2001) (Figure 1C, a). Interestingly, the region of insulin immunostaining was colocalized with ELKS (Figure 1C, b), although the ELKS seemed to be more widely distributed than insulin. On the other hand, the immunostaining pattern of syntaxin 1 differed from these but was seen on the entire cellular plasma membrane (our unpublished data), as described previously (Nagamatsu *et al.*, 1996).

We intended to confirm that ELKS is colocalized with insulin granules by immunogold electron microscopy by using anti-ELKS pAb and anti-insulin mAb (Figure 2). Different-sized colloidal gold particles (12 and 18 nm in diameter) were used to distinguish between the localization of ELKS and insulin. At the ultrastructural level in the section of rat pancreas, the immunoreactivity of ELKS (small gold particles, 12 nm) was frequently detected close to insulin (large gold particles,18 nm)-containing granule docked on the plasma membrane facing blood capillary (arrows). Thus, the immunoelectron results support our confocal microscopy data, indicating that ELKS colocalizes with the docking sites of insulin granules, and, in particular, gathers on blood capillaries.

**ELKS Is Unevenly Distributed in Separated Clusters in the Plasma Membrane of MIN6 $\beta$ Cells**

To investigate the function of ELKS, we used MIN6 $\beta$ cells, in which insulin release responds to the physiological range of glucose (Miyazaki *et al.*, 1990), and the expression pattern of the SNAREs is the same as that in primary $\beta$ cells (Nagamatsu *et al.*, 1999; Daniel *et al.*, 1999). We examined the expression of CAST isoforms in MIN6 cells by means of immunoblotting. As shown in Figure 3A, a band of ELKS protein was detected in MIN6 cells and rat brain (used as a

A
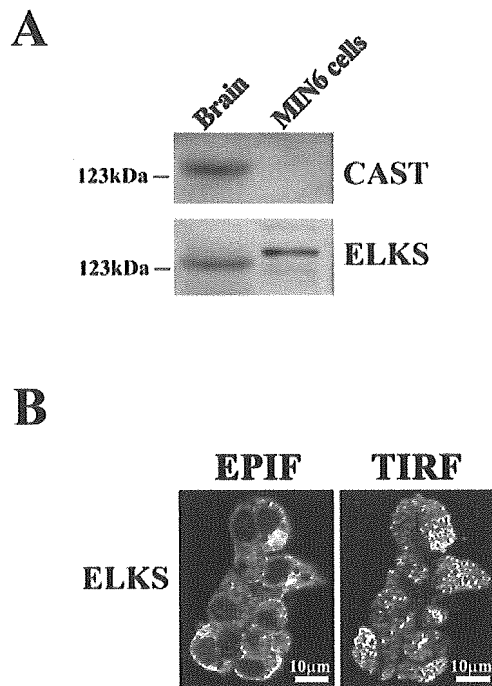


**Figure 3.** ELKS is present in MIN6 β cells. (A) Immunoblot analysis of CAST and ELKS proteins. The homogenates of rat brain (used as a positive control) and MIN6 β cells (20 μg of each protein) were analyzed by immunoblotting by using anti-CAST or anti-ELKS pAbs. Note that MIN6 cells expressed ELKS but not CAST. (B) Immunofluorescence staining of MIN6 cells with anti-ELKS pAb observed by EPIF microscopy and TIRFM. Cells were fixed and immunostained using anti-ELKS pAb and Alexa Fluor 488-conjugated anti-rabbit secondary antibody. EPIF images were observed by inverted EPIF microscopy, and TIRF images were observed by simply shifting the mirror in the same cells. Bars, 10 μm.

positive control), but a band of CAST was not detected in MIN6 cells. Distinct gel mobility (~130–140 kDa) also was observed in MIN6 cells, as well as in islets, which may reflect the β cell-specific splice variants of ELKS, as described above. Thus, MIN6 cells predominantly expressed ELKS but not CAST, which is in agreement with the results observed in rat islets.

To determine the subcellular localization of ELKS in MIN6 cells, the cells were fixed, immunostained with anti-ELKS pAb, and observed by both EPIF (common) microscopy and TIRFM of the same cell. Under EPIF microscopy, the immunofluorescence of ELKS was observed as dots primarily in not only the subplasmalemmal region but also the cytosol (Figure 3B, EPIF). TIRFM showed that the immunofluorescence of ELKS was unevenly and locally distributed in separate clusters in the plasma membrane (Figure 3B, TIRFM). Thus, the distribution pattern of ELKS clusters in the plasma membrane was regional and restricted.

*Site of ELKS Clusters Is Mostly Consistent with Docking Sites of Insulin Granules*

To determine the relationship between the site of docked insulin granules and that of ELKS clusters, we performed the double labeling for insulin and ELKS and observed them by TIRFM. As shown in Figure 4A, the spots for ELKS (green) were associated with areas for insulin granules, although these spots seem to be enlarged because of the
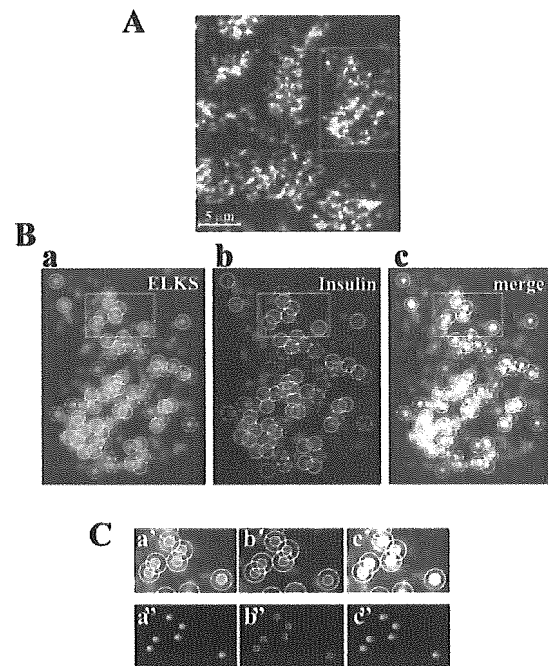
**Figure 4.** Colocalization of ELKS clusters and insulin granules in the plasma membrane of MIN6 cells analyzed by TIRFM. (A) Cells were fixed and double immunostained using anti-ELKS pAb, anti-insulin mAb, and secondary antibodies (Alexa Fluor-488-conjugated anti-rabbit and Alexa Fluor-546-conjugated anti-mouse antibodies). The colocalization of ELKS clusters (green) and insulin granules (red) is demonstrated by the overlap (yellow) of green and red channel images. (B) Most ELKS clusters (a, green) corresponded to sites of docked insulin granules (b, red). Box in the above-mentioned image indicates the region that is magnified below. Each circle (1 μm in diameter) in the green channel corresponds to the circle in the red channel. Solid circles represent the colocalization of ELKS clusters and insulin granules (positive). Dotted circles indicate observed ELKS clusters but not insulin granules (negative). Dashed circles indicate ELKS clusters with only a partially corresponding overlap (neutral). (C) Boxes in the above-mentioned images indicate regions that are magnified below. Inner circles (400 nm in diameter) were drawn around fluorescent spots in each image (a′, b′, and c′). Sizes of circles in images (a′) and (b′) were reduced to 64% (257 nm in diameter) and 68% (270 nm in diameter), respectively, to correct to the real diameters (a″ and b″), and these were transferred to identical pixel localizations (c″). Circles of ELKS clusters (green) and insulin granules (red) overlapped (rated as positive).

fluorescence of Alexa Fluor, and the diffraction-limited resolution of the objective. To correct judgment for rating the association of ELKS clusters with insulin granules, we corrected the apparent size of TIRF image to real size by using a formula based on the PSF, which was determined by measuring the diameter of fluorescent beads, as described previously (Ohara-Imaizumi *et al.*, 2004a) (see *Materials and Methods*). Indeed, the diameter of insulin granules observed in the TIRF image was 425 ± 19 nm (n = 6 cells), although the real size of insulin granules was calculated as 270 ± 30 nm, by use of a formula based on PSF, which agreed well with the value (289 nm) measured by electron microscopy of mouse pancreas (Dean, 1973). Similarly, the real diameter of the ELKS clusters was calculated as 257 ± 35 nm, on the basis of the apparent size of ELKS clusters (417 ± 21 nm, n = 6 cells). To correct the apparent sizes to real sizes based on these values, circles (400 nm in diameter) drawn around
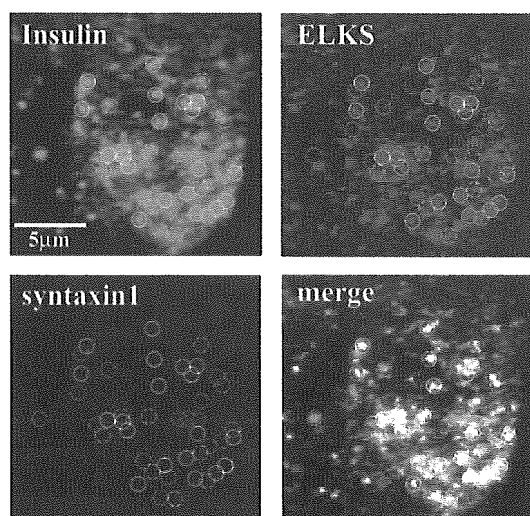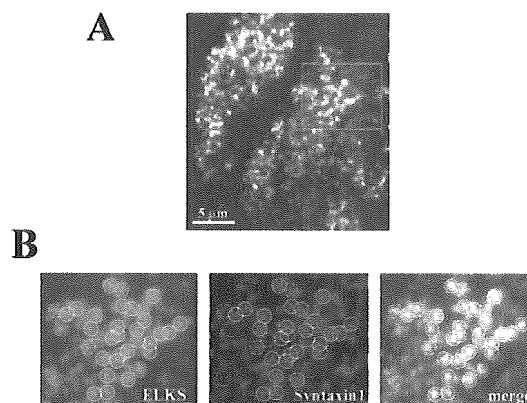
Figure 5. Insulin granules are preferentially docked to ELKS clusters colocalized with syntaxin 1 clusters. Cells were fixed and triple immunostained using rabbit anti-ELKS pAb, mouse anti-syntaxin 1 mAb, guinea pig anti-insulin pAb, and secondary antibodies (Alexa Fluor-546–conjugated anti-rabbit, Alexa Fluor-633–conjugated anti-mouse, and fluorescein-conjugated anti-guinea pig antibodies) and then were observed using TIRFM with an arc-lamp source. Colocalization was rated as described in Figure 4. Solid circles (1 μm in diameter) represent the insulin granules colocalized with ELKS and syntaxin 1 clusters. Dotted circles indicate observed insulin granules not colocalized with syntaxin 1 and ELKS clusters. Dashed circles indicate insulin granules with ELKS clusters or syntaxin 1 clusters.



Figure 6. Colocalization of ELKS and syntaxin 1 clusters in the plasma membrane. (A) Cells were fixed and double immunostained using anti-ELKS pAb, anti-syntaxin 1 mAb, and secondary antibodies (Alexa Fluor-488–conjugated anti-rabbit and Alexa Fluor-546–conjugated anti-mouse antibodies). The colocalization of ELKS clusters (green) and syntaxin 1 clusters (red) is demonstrated by the overlap (yellow) of red and green channel images. (B) A majority of ELKS clusters (green) colocalized with syntaxin 1 clusters (red). Box in the above-mentioned image indicates the region that is magnified below. Each circle (1 μm in diameter) in the green channel corresponds to the circle in the red channel. Colocalization was rated as described in Figure 4. The real diameters of ELKS and syntaxin 1 clusters were calculated as 257 ± 35 and 280 ± 37 nm on the basis of the apparent size of the ELKS and syntaxin 1 clusters (417 ± 21 and 431 ± 24 nm, respectively, n = 6 cells). Solid circles represent the colocalization of ELKS and syntaxin 1 clusters (positive). Dotted circles indicate observed ELKS clusters but not syntaxin 1 clusters (negative). Dashed circles indicate ELKS clusters with only partially corresponding overlap (neutral).

fluorescent spots for insulin granules and ELKS clusters observed in TIRF images (Figure 4B) were reduced to 68 and 64%, respectively (Figure 4C). As shown in the drawing in Figure 4C, ELKS clusters were precisely localized with insulin granules. By using these corrections, we could demonstrate that ELKS clusters were rated to be associated with granule (positive) when their signals fully overlapped. Clusters that overlapped less were rated as negative, and partially overlapping clusters were rated as neutral (Figure 4B). As shown in Figure 4B, 60.5 ± 2.2 and 24.5 ± 4.7% of all labeled ELKS clusters fully or partially corresponded to the docking sites of insulin granules, respectively, whereas 15.1 ± 4.4% of ELKS clusters did not correspond to the docking sites of insulin granules (n = 13 cells). Thus, ~85% of ELKS clusters corresponded to sites of docked insulin granules. Although some of these clusters may have been colocalized with insulin granules, at least 60% of ELKS clusters were perfectly matched to the sites of docked insulin granules, thus indicating that ELKS is involved in physiological interaction with insulin granule on the docking site.

We then examined the interaction between insulin granules docking sites and ELKS and syntaxin 1 clusters, by triple immunostaining observed using TIRFM with an arc-lamp source. As shown in Figure 5, a majority of the insulin granules colocalized with either ELKS or syntaxin 1 clusters. Among them, 46.1 ± 2.9% of insulin granules (n = 12 cells) docked on the sites of ELKS clusters colocalizing with syntaxin 1.

### Colocalization of ELKS and Syntaxin 1 Clusters in the Plasma Membrane

We examined the colocalization of ELKS and syntaxin 1. As shown in Figure 6A, syntaxin 1 clusters (red) were more

enriched and evenly distributed on the entire plasma membrane than are ELKS clusters (green), which were less dense and unevenly distributed on the plasma membrane. The number of ELKS clusters on the plasma membrane was 115.5 ± 6.8 per 200 μm² (n = 15 cells), whereas the number of syntaxin 1 clusters was 236.8 ± 7.2 per 200 μm² (n = 15 cells; p < 0.001). Detailed examination of A by correction of the apparent size of the TIRF image to real size by using a formula based on PSF, revealed that the majority of ELKS clusters colocalized with the syntaxin 1 clusters (Figure 6B). Of the labeled ELKS clusters, 69.8 ± 6.8% of all labeled ELKS clusters was fully corresponded to the syntaxin 1 clusters (positive) (n = 15 cells), and 13.9 ± 2.8% of the ELKS clusters were only partially overlapped with syntaxin 1 cluster (rated as neutral). Thus, ~84% of ELKS clusters colocalized with syntaxin1 clusters. This uneven distribution of ELKS clusters colocalized with syntaxin 1 clusters seems to indicate that the fusion site of docked insulin granules is restricted to ELKS clusters.

### Fusion of Insulin Granules Frequently Occurred on ELKS Clusters

To determine whether the fusion of insulin granules occurred on the ELKS clusters, we analyzed the interaction between the docking/fusion of GFP-tagged insulin granules and ELKS clusters labeled by TAT-conjugated, Cy3-labeled mAb, by using living MIN6 cells and TIRF images. As has been demonstrated previously (Ohara-Imaizumi *et al.*, 2004a), TAT-conjugated Cy3-labeled anti-ELKS mAb is rapidly transduced into cells (our unpublished data). We ensured that the TAT-conjugated, Cy3-labeled anti-ELKS mAb